*Lecture notes on*:

# Accidental and symmetry-enforced band crossings in topological semimetals

*Topological Matter School 2018, San Sebastian, Spain*

**Andreas P. Schnyder**

a.schnyder@fkf.mpg.de

August 30, 2018

*Max-Planck-Institut für Festkörperforschung*
*Heisenbergstrasse 1, D-70569 Stuttgart, Germany*

**Contents**

## I. INTRODUCTION

The famous non-crossing theorem by Wigner and von Neumann [1] states that electronic bands (i.e., Bloch states) with the same symmetry cannot be degenerate at a generic point in the Brillouin zone (BZ), which prevents the formation of band crossings. Instead, when two Bloch bands of the same symmetry approach each other at a generic momentum, they start to hybridize and undergo an avoided level crossing. However, the non-crossing theorem does not apply to bands with non-trivial wavefunction topology, which can form topologically protected band degeneracies [2–7]. When these band crossings are in the vicinity of the Fermi energy, they lead to a range of interesting phenomena, such as arc and drumhead surface states [8–14], transverse topological currents [5, 6, 15], and anomalous magnetoelectric responses [16], which could potentially be utilized for device applications [17, 18].

There are two different types of topological band crossings, namely, accidental band crossings and symmetry-enforced band crossings. The former are protected by symmorphic crystal symmetries and are only perturbatively stable [19–21]. That is, they can be adiabatically removed by large symmetry-preserving deformations of the Hamiltonian, for example, through pair annihilation. Examples of accidental band crossings include Dirac points and Dirac lines that are protected by space-time inversion, reflection, or rotation symmetry [22–27]. Accidental band crossings also occur in the Bogoliubov quasiparticle spectra of superconductors [28–30]. Symmetry-enforced band crossings [16, 31–42], on the other hand, arise in the presence of *nonsymmorphic* symmetries and are globally stable, i.e., they cannot be removed even by large deformations of the Hamiltonian. In other words, these band crossings are required to exist due to nonsymmorphic symmetries alone, independent of the chemical composition and other details of the material.

In these lectures we will discuss both types of band crossings, first focusing on accidental band crossing in Sec. II and then studying symmetry-enforced band crossings in Sec. III. A particular focus will be on nodal-line semimetals, where the band crossings occur along one-dimensional lines in the BZ, close to or at the Fermi energy. How such line crossings arise in the presence of (glide) reflection symmetries will be studied in detail.

In Sec. II A we will begin by deriving a classification of accidental band crossings protected by reflection symmetry, time-reversal symmetry, and/or particle-hole symmetry. As concrete examples of such accidental band crossings, we will consider, among others, Weyl and nodal-line semimetals (Secs. II C 2 and II C 3), as well as a spin-triplet superconductor (Sec. II C 4). For these examples

we will discuss the bulk-boundary correspondence, which relates the nontrivial topology of the band crossing in the bulk to the appearance of surface states.

In Sec. III we will first explain some general properties of non-symmorphic symmetries, show how these can lead to symmetry-enforced band crossings, and derive therefrom a strategy for the discovery of new topological semimetals. Subsequently, three examples of non-symmorphic band crossing will be discussed: Weyl points protected by six-fold screw rotation in Sec. III B 2, Weyl lines protected by glide reflection in Sec. III B 1, and Dirac lines protected by off-center symmetries in Sec. III B 3. We will also discuss how nonsymmorphic symmetries lead to tightened filling constraints for the existence of band insulators (Sec. III C).

### 1. *Bloch bands of solids*

According to the band theory of solids [43], the electronic wavefunctions $\psi$ in a crystal can be classified by their crystal momentum $\boldsymbol{k}$, which is defined in a periodic Brillouin zone (BZ). Bloch's theorem tells us that $\psi$ can be expressed in terms of Bloch states $|u_m(\boldsymbol{k})\rangle$, which are defined in a single unit cell of the crystal. These Bloch states are eigenstates of the Bloch Hamiltonian $H(\boldsymbol{k})$,

$$H(\boldsymbol{k})\,|u_m(\boldsymbol{k})\rangle = E_m(\boldsymbol{k})\,|u_m(\boldsymbol{k})\rangle\,, \tag{1.1}$$

where $m$ represents the band index. The eigenvalues $E_m(\boldsymbol{k})$ in the above equation are called Bloch bands and the set $\{E_m(\boldsymbol{k})\}$ is referred to as the band structure of the solid.

In this lecture we are interested in the crossings between two different bands, $E_m(\boldsymbol{k})$ and $E_{m'}(\boldsymbol{k})$, say. That is, we want to know under which conditions the the two energies $E_m(\boldsymbol{k})$ and $E_{m'}(\boldsymbol{k})$ become degenerate at certain points or lines in the BZ. The main focus will be on electronic band structures of solids. However, the band crossings discussed here can also occur in different contexts, for example, for photonic bands of dielectric superlattices [44], for phonon bands in crystals, for magnon bands in ordered antiferromagnets [45], or for Bogoliubov quasiparticle bands in superconductors (see Sec. II C 4).

## II. ACCIDENTAL BAND CROSSINGS

Accidental band crossings occur, for example, when a hole-like and electron-like parabolic band in a two-dimensional material overlap, forming two band crossings, as shown in Fig. 1. This band crossing is stable if the two bands have a non-trivial topology and/or opposite symmetry. In general these accidental crossings share the following features:

- They are protected by *symmorphic* crystal symmetries and/or nonspatial symmetries. Here, symmorphic symmetry means a symmetry wich leaves at least one point of the real-space crystal invariant. Symmorphic symmetries are point-group symmetries of the crystal, such as rotation or reflection. Nonspatial symmetry refers to a symmetry that dose not transform different lattice sites into each other. I.e., a symmetry that acts locally in real space, such as time-reversal or particle-hole symmetry.

- Accidental band crossings exhibit local topological charges. These topological charges are defined in terms of contour integrals, e.g.,

$$n_{\text{top}} = \frac{1}{2\pi} \oint_{\mathcal{C}} \mathcal{F}(\boldsymbol{k})\, d\boldsymbol{k} \;\in\; \mathbb{Z}, \tag{2.1}$$

  where the integration is along the contour $\mathcal{C}$, which encloses the band crossing point or line. Here, $\mathcal{F}(\boldsymbol{k})$ represents a general curvature function, such as the Berry curvature or

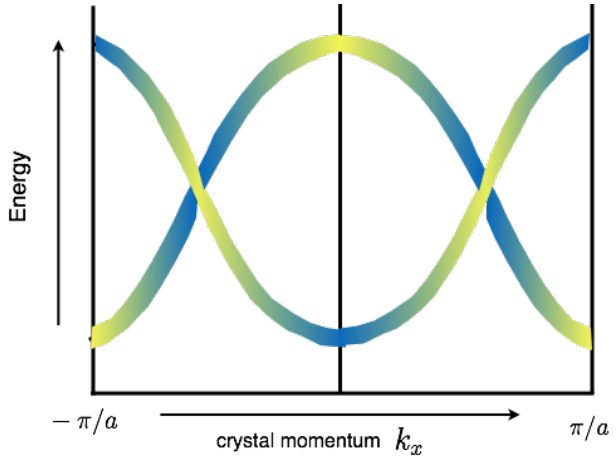


FIG. 1: *Accidental band crossings*. When an electron- and hole-like band of different symmetry overlap, they form two accidental band crossings. The color shading indicates some "pseudo-spin" degree of freedom of the Bloch states $|u_n(\boldsymbol{k})\rangle$, which depends on crystal momentum $\boldsymbol{k}$.

the winding number density. These topological charges are quantized to integer values, i.e., $n_{\text{top}} \in \mathbb{Z}$. For point crossings, the sum of the topological charges of all crossings formed by a given pair of bands needs to be zero, due to a fermion-doubling theorem [46].

- Accidental band crossings are only perturbatively stable. That is, small symmetry-preserving perturbations can move the band crossings in the BZ, but cannot remove them, by opening up a gap. However, large symmetry-preserving deformations can completely remove the band crossings. E.g., for point crossings one can pair annihilate two point crossings with opposite topological charge by a large symmetry-preserving deformation.

It follows from the last point above, that classifications of accidental band crossings based on symmetry and topology only tell us whether for a given set of symmetries a band crossing is *possible*. I.e., these classifications only tell us whether a given set of symmetries protect band crossings or not. They do not tell us whether these crossings actually occur, which depends on the detailed energetics of the bands (i.e., on how the bands disperse through the BZ).

### A. Classification of band crossings

Topological band crossings of the accidental type can be classified using the Dirac-matrix Hamiltonian method [2, 19, 47–49]. This method relies on the fact that close to a band crossing the bands are linearly dispersing. Therefore, the Bloch Hamiltonian $H(\boldsymbol{k})$, Eq. (1.1), in the vicinity of the band crossing can be approximated by a Dirac Hamiltonian, e.g.,

$$H_D(\boldsymbol{k}) = \sum_{j=1}^{d} k_j \gamma_j, \tag{2.2}$$

where $d$ is the spatial dimension and the $\gamma$-matrices $\gamma_j$ obey the anti-commutation relations (see Appendix B)

$$\{\gamma_i, \gamma_j\} = 2\delta_{ij}\mathbb{1}, \qquad j = 0, 1, \ldots, d. \tag{2.3}$$

Using Eq. (2.3), we find that $H_D^2 = \sum_{j=1}^{d} k_j^2 \mathbb{1}$. Hence, the energy spectrum of $H_D(\boldsymbol{k})$ is given by

$$E = \pm\sqrt{\sum_{j=1}^{d} k_j^2}, \tag{2.4}$$

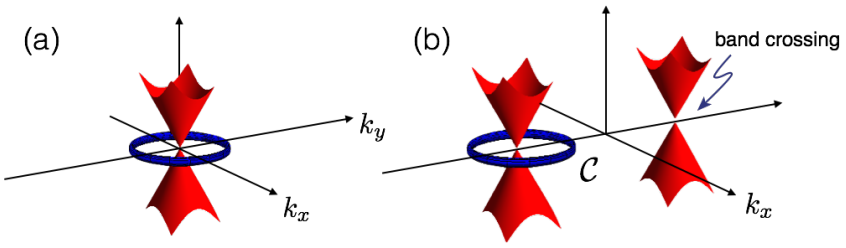


FIG. 2: *Symmetry transformation of band crossings*. The classification of stable band crossings depends on how the band crossings transform under nonspatial (antiunitary) symmetries. (a) The band crossing is left invariant under nonspatial symmetries. (b) Two band crossings are pairwise related by the nonspatial symmetries, which map $\boldsymbol{k} \to -\boldsymbol{k}$.

which exhibits a band crossing at $\boldsymbol{k} = 0$, where the bands become degenerate with $E = 0$. (I.e., the Dirac Hamiltonian has no gap.) The Dirac-matrix Hamiltonian method analyzes the stability of the gapless Dirac-Hamiltonian (2.2) against gap opening deformations. That is, one studies whether there exists a gap-opening mass term $m\gamma_0$, i.e., an additional gamma matrix $\gamma_0$ with $\{\gamma_0, \gamma_j\} = 0$ ($j = 1, 2, \ldots, d$), with which $H_D(\boldsymbol{k})$ can be deformed. If such a mass term exists, then the band crossing can be removed. I.e., by adding $m\gamma_0$ to $H_D$ the spectrum deforms into $E = \pm\sqrt{m^2 + \sum_{j=1}^{d} k_j^2}$, which has no band crossing anymore at $\boldsymbol{k} = 0$. This indicates that the band crossing is topologically trivial. However, if there does not exist an additional gamma matrix $\gamma_0$, then the band crossing is topologically nontrivial and stable against deformations.
The classification of band crossings is done in terms of the following three characteristics (cf. Table I):

(i) Spatial and nonspatial symmetries of the Bloch Hamiltonian $H(\boldsymbol{k})$.

(ii) The co-dimension $p = d - d_{BC}$ of the band crossing, where $d_{BC}$ is the dimension of the band crossing. (I.e., $d_{BC} = 0$ for point crossings, $d_{BC} = 1$ for line crossings, etc.)

(iii) How the band crossing transforms under the nonspatial (antiunitary) symmetries. That is, we need to distinguish whether the band crossing is mapped onto itself under the nonspatial symmetries or not, see Fig. 2. That is, we need to differentiate between band crossings at high-symmetry points and off high-symmetry points of the BZ.

Let us first discuss how the spatial and nonspatial symmetries restrict the form of the Dirac Hamiltonian (2.2).

### 1. Symmetry operations

We consider the classification in terms of both nonspatial and spatial symmetries.

*a. Nonspatial symmetries.* Nonspatial symmetries are symmetries that act locally in real space, i.e., they do not transform different lattice sites into each other. There are three different nonspatial symmetries that need to be considered: antiunitary time-reversal symmetry (TRS) and particle-hole symmetry (PHS), as well as chiral (i.e., sublattice symmetry) [2, 50]. Here, "anntiuniatary" refers to the fact that these symmetries can be written as a product of a unitary matrix $U$ with the complex conjugation operator $\mathcal{K}$. In momentum space, time-reversal and particle-hole symmetry act on the Bloch (or Bogoliubov-de Gennes) Hamiltonian as

$$\mathcal{T}^{-1}H(-\boldsymbol{k})\mathcal{T} = +H(\boldsymbol{k}), \quad \text{and} \quad \mathcal{C}^{-1}H(-\boldsymbol{k})\mathcal{C} = -H(\boldsymbol{k}), \tag{2.5a}$$

respectively, where $\mathcal{T}$ and $\mathcal{C}$ are the antiunitary operators for time-reversal and particle-hole symmetry. Both $\mathcal{T}$ and $\mathcal{C}$ can square either to $+1$ or $-1$, depending on the type of the symmetry (see last three columns of Table I). Chiral symmetry, on the other hand, is implemented by[1]

$$\mathcal{S}^{-1}H(\boldsymbol{k})\mathcal{S} = -H(\boldsymbol{k}), \tag{2.5b}$$

where $\mathcal{S}$ is a unitary operator. Symmetries (2.5) define the ten Altland-Zirnbauer (AZ) symmetry classes (i.e., the "ten-fold way") [2, 51, 52], which are listed in Table I. The first column in Table I gives the name of the ten AZ symmetry classes. The labels $T$, $C$, and $S$ in the last three columns indicate the presence ("+", "−", and "1") or absence ("0") of time-reversal symmetry, particle-hole symmetry and chiral symmetry, respectively, as well as the sign of the squared symmetry operators $\mathcal{T}^2$ and $\mathcal{C}^2$.

Combining Eqs. (2.5) with Eq. (2.2), we find that when the Dirac Hamiltonian obeys TRS, PHS, or chiral symmetry, the gamma matrices in Eq. (2.2) must satisfy

$$\{\gamma_i, \mathcal{T}\} = 0, \quad [\gamma_i, \mathcal{C}] = 0, \quad \{\gamma_i, \mathcal{S}\} = 0, \tag{2.6}$$

where $i = 1, 2, \ldots, d$. Similarly, any mass term $m\gamma_0$ that leads to the opening of a gap at the band crossing must satisfy

$$[\gamma_0, \mathcal{T}] = 0, \quad \{\gamma_0, \mathcal{C}\} = 0, \quad \{\gamma_0, \mathcal{S}\} = 0. \tag{2.7}$$

[1] Note that combining TRS with PHS yields a chiral symmetry.

TABLE I: Classification of stable band crossings in terms of the ten AZ symmetry classes [2, 53], which are listed in the first column. The first and second rows give the co-dimensions $p = d - d_{BC}$ for band crossings at high-symmetry points [Fig. 2(a)] and away from high-symmetry points of the BZ [Fig. 2(b)], respectively.

| at high-sym. point<br>off high-sym. point | $p$=8<br>$p$=2 | $p$=1<br>$p$=3 | $p$=2<br>$p$=4 | $p$=3<br>$p$=5 | $p$=4<br>$p$=6 | $p$=5<br>$p$=7 | $p$=6<br>$p$=8 | $p$=7<br>$p$=1 | T | C | S |
|---|---|---|---|---|---|---|---|---|---|---|---|
| A | 0 | $\mathbb{Z}$ | 0 | $\mathbb{Z}$ | 0 | $\mathbb{Z}$ | 0 | $\mathbb{Z}$ | 0 | 0 | 0 |
| AIII | $\mathbb{Z}$ | 0 | $\mathbb{Z}$ | 0 | $\mathbb{Z}$ | 0 | $\mathbb{Z}$ | 0 | 0 | 0 | 1 |
| AI | 0 | 0[a] | 0 | $2\mathbb{Z}$ | 0 | $\mathbb{Z}_2$[a,b] | $\mathbb{Z}_2$[b] | $\mathbb{Z}$ | + | 0 | 0 |
| BDI | $\mathbb{Z}$ | 0 | 0[a] | 0 | $2\mathbb{Z}$ | 0 | $\mathbb{Z}_2$[a,b] | $\mathbb{Z}_2$[b] | + | + | 1 |
| D | $\mathbb{Z}_2$[b] | $\mathbb{Z}$ | 0 | 0[a] | 0 | $2\mathbb{Z}$ | 0 | $\mathbb{Z}_2$[a,b] | 0 | + | 0 |
| DIII | $\mathbb{Z}_2$[a,b] | $\mathbb{Z}_2$[b] | $\mathbb{Z}$ | 0 | 0[a] | 0 | $2\mathbb{Z}$ | 0 | − | + | 1 |
| AII | 0 | $\mathbb{Z}_2$[a,b] | $\mathbb{Z}_2$[b] | $\mathbb{Z}$ | 0 | 0[a] | 0 | $2\mathbb{Z}$ | − | 0 | 0 |
| CII | $2\mathbb{Z}$ | 0 | $\mathbb{Z}_2$[a,b] | $\mathbb{Z}_2$[b] | $\mathbb{Z}$ | 0 | 0[a] | 0 | − | − | 1 |
| C | 0 | $2\mathbb{Z}$ | 0 | $\mathbb{Z}_2$[a,b] | $\mathbb{Z}_2$[b] | $\mathbb{Z}$ | 0 | 0[a] | 0 | − | 0 |
| CI | 0[a] | 0 | $2\mathbb{Z}$ | 0 | $\mathbb{Z}_2$[a,b] | $\mathbb{Z}_2$[b] | $\mathbb{Z}$ | 0 | + | − | 1 |

[a] For these entries there can exist bulk band crossings away from high-symmetry points that are protected by $\mathbb{Z}$ invariants inherited from classes A and AIII. (TRS or PHS does not trivialize the $\mathbb{Z}$ invariants.)

[b] $\mathbb{Z}_2$ invariants protect only band crossings of dimension zero at high-symmetry points.

*b. Spatial symmetries.* Spatial symmetries are symmetries that act non-locally in position space, i.e., they transform different lattice sites into each other. Point-group symmetries are an example of spatial symmetries. Here, we shall focus on reflection symmetries with the unitary operator $R$. For concreteness we assume that $R$ lets $x \to -x$. The invariance of the Bloch Hamiltonian (1.1) under this reflection implies

$$R^{-1} H(-k_1, \tilde{\boldsymbol{k}}) R = H(k_1, \tilde{\boldsymbol{k}}), \tag{2.8}$$

where $\tilde{\boldsymbol{k}} = (k_2, \ldots, k_d)$ and the unitary reflection operator $R$ can only depend on $k_1$, since it is symmorphic [cf. Eq. (3.10)]. Note that for spin-1/2 particles (e.g., Bloch electrons with spin-orbit

coupling) $R$ transforms the spin degree of freedom as

$$R\hat{S}_x R^{-1} = \hat{S}_x \quad \text{and} \quad R\hat{S}_{y,z} R^{-1} = -\hat{S}_{y,z}, \tag{2.9}$$

where $\hat{S}_i = \frac{\hbar}{2}\hat{\sigma}_i$ is the spin operator. Hence, the spin part of $R$ is given by $i\sigma_x$ [2]. In general, $R$ contains also an internal part which rearranges the positions of the atoms in the unit cell.
Combining Eqs. (2.8) with Eq. (2.2), we find that when the Dirac Hamiltonian obeys reflection symmetry, the gamma matrices in Eq. (2.2) must satisfy

$$\{\gamma_1, R\} = 0, \quad [\gamma_j, R] = 0, \quad \text{where } j = 2, 3, \ldots, d, \tag{2.10}$$

and the mass term must satisfy $[\gamma_0, R] = 0$.

### B. Band crossings at high-symmetry points

We will now use the Dirac-matrix Hamiltonian method[3] to classify one-dimensional band crossings at high-symmetry points of the BZ, i.e., at time-reversal invariant momenta (TRIMs) of the BZ, e.g., the $\Gamma$ point. This classification approach consists of the following steps:

1. Write down a $d$-dimensional gapless Dirac Hamiltonian $H_D$ of the form of Eq. (2.2), that is invariant under all the considered symmetries. The matrix dimension of the gamma matrices should be minimal, i.e., large enough such that all symmetries can be implemented in a nontrivial way, but not larger.

2. Check whether there exists a symmetry-allowed mass term $m\gamma_0$, which anticommutes with $H_D$. If *yes*, then the band crossing can be gapped out. This indicates that the band crossing is topologically trivial, which is labelled by "0" in Table I. If *no*, then the band crossing is topologically stable (i.e., protected by the symmetries), which is labelled by "$\mathbb{Z}$ or "$\mathbb{Z}_2$" in Table I.

3. To determine whether there is a single or multiple band crossings protected by the symmetries, we have to consider multiple copies of the Dirac Hamiltonian $H_D$. For example,

[2] The reason to include the factor $i$ here is to ensure that $R^2 = -1$, since $R^2$ effectively corresponds to a spin rotation by $2\pi$. However, in general, there is a phase ambiguity in the definition of $R$, since a phase can be absorbed in the electronic creation/annihilation operators.

[3] This approach is closely related to the problem of Clifford algebra extensions [2, 21, 49], which puts it on a rigorous footing.

doubled versions of $H_D$ can be obtained as

$$H_D^{\text{db}} = \sum_i k_{n_i} \gamma_{n_i} \otimes \sigma_z + \sum_{\text{remain}} k_{n_j} \gamma_{n_j} \otimes \mathbb{1}, \tag{2.11}$$

where the first summation is over an arbitrary subset $n_i \subseteq \{1, 2, ..., d\}$ and the second summation is over the complement of this subset. We then have to check whether there exist gap-opening terms for these enlarged Dirac Hamiltonians. If there exists a mass term for all possible versions of $H_D^{\text{db}}$, then the band crossing is classified by a $\mathbb{Z}_2$ invariant. If the band crossing is stable for an arbitrary number of copies of $H_D$, then it is classified by a $\mathbb{Z}$ number[4], see Table I.

To make this more explicit, let us discuss some specific cases.

### 1. *Class A in* $d = 2$

First, we consider a band crossing in a two-dimensional system without any symmetries, corresponding to class A in Table I. The generic low-energy Hamiltonian for a such a band crossing at $\boldsymbol{k} = 0$ reads $\mathcal{H}_{2D}^A = \sum_{\boldsymbol{k}} \Psi_{\boldsymbol{k}}^\dagger H_{2D}^A \Psi_{\boldsymbol{k}}$, where

$$H_{2D}^A = k_x \sigma_x + k_y \sigma_y. \tag{2.12}$$

and $\Psi_{\boldsymbol{k}} = (c_{1\boldsymbol{k}}, c_{2\boldsymbol{k}})^T$ is a spinor with two orbital degrees of freedom, e.g., $s$ and $p$ orbitals. Since this band crossing can be gapped out by the mass term $m\sigma_z$, it is topologically trivial and therefore unstable. This is indiacted by a "0" in the fourth column of Table I.

### 2. *Class A in* $d = 3$

Next, we study a zero-dimensional band crossing in three-dimensions without any symmetries. This type of band crossing is realized in Weyl semimetals [2, 5, 8]. The low-energy Hamiltonian takes the form $\mathcal{H}_{3D}^A = \sum_{\boldsymbol{k}} \Psi_{\boldsymbol{k}}^\dagger H_{3D}^A \Psi_{\boldsymbol{k}}$, with

$$H_{3D}^A = k_x \sigma_x + k_y \sigma_y + k_z \sigma_z. \tag{2.13}$$

[4] To show this, use a proof by induction.

It is impossible to find a mass term for this Hamiltonian, because there exist only three gamma matrices of rank 2. (There exists no "fourth Pauli matrix" that anticommutes with $H_{3D}^{A}$.) Therefore, the band-crossing is stable. To determine whether the Weyl crossing (2.13) has a $\mathbb{Z}$ or $\mathbb{Z}_2$ classification, we need to consider all possible doubled versions of $H_{3D}^{A}$, cf. Eq. (2.11). We can consider, for example, the following doubled version of $H_{3D}^{A}$

$$H_{3D}^{A,\mathrm{db1}} = k_x\sigma_x \otimes \sigma_z + k_y\sigma_y \otimes \sigma_0 + k_z\sigma_z \otimes \sigma_0, \tag{2.14}$$

where $\otimes$ denotes the tensor product between two Pauli matrices (cf. Appendix B). For this doubled version of $H_{3D}^{A}$, there exist two mass terms, e.g., $\sigma_x \otimes \sigma_x$ and $\sigma_x \otimes \sigma_y$, which gap out the band crossing. However, there exists another doubled version of $H_{3D}^{A}$, namely

$$H_{3D}^{A,\mathrm{db2}} = k_x\sigma_x \otimes \sigma_0 + k_y\sigma_y \otimes \sigma_0 + k_z\sigma_z \otimes \sigma_0, \tag{2.15}$$

whose band crossing is stable. We find that there does not exist any mass term for $H_{3D}^{A,\mathrm{db2}}$, which gaps out the band crossing. Since we have found one doubled version of $H_{3D}^{A}$ which has a stable (four-fold degenerate) band crossing, we conclude that Weyl band crossings exhibit a $\mathbb{Z}$ classificaiton. (One can show that there exist also multiple copies of $H_{3D}^{A}$ with stable band crossings.) This is indicated by the label "$\mathbb{Z}$" in the fifth column of Table I.

The Weyl points described by Eq. (2.13) are monopoles of Berry flux, i.e., they realize (anti-)hedgehog defects of the Berry curvature. The stability of these Weyl points is guaranteed by a quantized Chern number (see Sec. II C 2).

### 3. *Class A + R in* $d = 2$

Let us now add reflection symmetry to the game. We consider again a two-orbital system with the low-energy Hamiltonian $\mathcal{H}_{2D}^{A+R} = \sum_{\boldsymbol{k}} \Psi_{\boldsymbol{k}}^{\dagger} H_{2D}^{A+R} \Psi_{\boldsymbol{k}}$, where

$$H_{2D}^{A+R} = k_x\sigma_x + k_y\sigma_y, \tag{2.16}$$

which is symmetric under reflection symmetry $R^{-1}H_{2D}^{A+R}(-k_x, k_y)R = H_{2D}^{A+R}(k_x, k_y)$, with $R = \sigma_y$. We observe that the only possible gap-opening mass term $m\sigma_z$, which anticommutes with $H_{2D}^{A+R}$, is symmetry forbidden, since it breaks reflections symmetry ($R^{-1}\sigma_z R = -\sigma_z$). Hence, the band-crossing of $H_{2D}^{A+R}$ at $\boldsymbol{k} = 0$ is stable and protected by reflection symmetry. We find that also the doubled version of $H_{2D}^{A+R}$,

$$H_{2D}^{A+R,\mathrm{db}} = k_x\sigma_x \otimes \sigma_0 + k_y\sigma_y \otimes \sigma_0, \tag{2.17}$$

is stable, since there exists no relfection-symmetric mass term. For example, $\hat{m} = \sigma_z \otimes \sigma_x$ breaks reflection, since $(\sigma_y \otimes \sigma_0)^{-1}\hat{m}(\sigma_y \otimes \sigma_0) \neq \hat{m}$. Therefore, the reflection-symmetric band crossing (2.16) has a $\mathbb{Z}$ classification. This is indicated by the label "$M\mathbb{Z}$" in the fifth column of Table VIII of Ref. [2].

#### 4. *Class AII in* $d = 2$

Next, we study a band crossing in two-dimensions with time-reversal symmetry ($\mathcal{T}^2 = -1$), corresponding to class AII in Table I. The low-energy Dirac Hamiltonian reads again

$$H_{2D}^{\mathrm{AII}} = k_x\sigma_x + k_y\sigma_y. \tag{2.18}$$

But now we impose time-reversal symmetry (2.5a) with the operator $\mathcal{T} = i\sigma_y\mathcal{K}$, which squares to $-1$ (class AII). This type of time-reversal symmetric band crossing is realized at the surface of three-dimensional topological insulators with spin-orbit coupling. The only possible mass term, which anticommutes with $H_{2D}^{\mathrm{AII}}$, is $m\sigma_z$. However, $m\sigma_z$ breaks time-reversal symmetry (since, $\mathcal{T}^{-1}m\sigma_z\mathcal{T} \neq m\sigma_z$) and is therefore forbidden by symmetry. Hence, Eq. (2.18) describes a topologically stable band crossing in class AII. Next, we examine different doubled versions of $H_{2D}^{\mathrm{AII}}$, i.e.,

$$H_{2D}^{\mathrm{AII,db}} = \begin{pmatrix} H_{2D}^{\mathrm{AII}} & 0 \\ 0 & H_{2D}^{\mathrm{AII}'} \end{pmatrix}, \tag{2.19}$$

where $H_{2D}^{\mathrm{AII}'} \in \{\pm k_x\sigma_x \pm k_y\sigma_y, \pm k_x\sigma_x \mp k_y\sigma_y\}$, see Eq. (2.11). (The time-reversal operator for these double Hamiltonians is $\mathcal{T} = i\sigma_y \otimes \sigma_0\mathcal{K}$.) It is not difficult to show that for each of the four versions of $H_{2D}^{\mathrm{AII,db}}$ there exists at least one symmetry-preserving mass term, wich gaps out the band crossing. For example, for the first version of $H_{2D}^{\mathrm{AII,db}}$ with $H_{2D}^{\mathrm{AII}'} = +k_x\sigma_x + k_y\sigma_y$, the mass term is $\sigma_z \otimes \sigma_y$. Thus, the band crossings described by $H_{2D}^{\mathrm{AII,db}}$ is unstable. Therefore, we conclude that Eq. (2.18) has a $\mathbb{Z}_2$ classification, see fourth column of Table I.

#### 5. *Class AII +* $R_+$ *in* $d = 3$

Next, we study the band crossing of a reflection symmetric three-dimensional Dirac semimetal with time-reversal symmetry ($\mathcal{T}^2 = -1$), which is described by $\mathcal{H}_{3D}^{\mathrm{AII+R}} = \sum_{\boldsymbol{k}} \Psi_{\boldsymbol{k}}^\dagger H_{3D}^{\mathrm{AII+R}} \Psi_{\boldsymbol{k}}$ with

$\Psi_{\boldsymbol{k}} = (c_{1\boldsymbol{k}}, c_{2\boldsymbol{k}}, c_{3\boldsymbol{k}}, c_{4\boldsymbol{k}})^T$ and

$$H_{3D}^{\mathrm{AII+R}} = k_x \sigma_x \otimes \sigma_z + k_y \sigma_y \otimes \sigma_0 + k_z \sigma_z \otimes \sigma_0. \tag{2.20}$$

Time-reversal and reflection symmetry operators are given by $\mathcal{T} = \sigma_y \otimes \sigma_0 \mathcal{K}$ and $R = \sigma_0 \otimes \sigma_x$, respectively. Because $\mathcal{T}^2 = -1$ and $[\mathcal{T}, R] = 0$, Hamiltonian (2.20) belongs to symmetry class AII with $R_+$ according to the nomenclature of Refs. [19, 47]. We observe that there exists no mass term which respects both time-reversal and reflection symmetry. Therefore, the band crossing (Dirac point) at $\boldsymbol{k} = 0$ of Eq. (2.20) is topologically stable. However, doubled versions of this Dirac point are unstable. Consider, for example, the doubled Hamiltonian $H_{3D}^{\mathrm{AII+R}} \otimes \sigma_0$, whose band crossing can be gapped out by the symmetry-preserving mass term $\sigma_x \otimes \sigma_x \otimes \sigma_y$. Hence, Eq. (2.20) has a $\mathbb{Z}_2$ classification, see sixth column of Table VIII of Ref. [2].

### C. Band crossings off high-symmetry points

In this section we classify band crossings that are located away from high-symmetry points, i.e., away from the TRIMs of the BZ, see Fig. 2(b). These band crossings can be moved around in the BZ, as they are not pinned at the TRIMs. They transform pairwise into each other by the nonspatial antiunitary symmetries (time-reversal and particle-hole symmetry). For this reason, we have to take into account the full momentum dependence of the Hamiltonian in the entire BZ. That is, within the Dirac-matrix Hamiltonian approach, we need to consider the following type of Hamiltonian [19]

$$H_D = \sum_{i=1}^{p-1} \sin k_i \gamma_i + (p - 1 - \sum_{i=1}^{p} \cos k_i) \tilde{\gamma}_0, \tag{2.21}$$

which contains the momentum-dependent mass term $\tilde{\gamma}_0$, cf. Eq. (2.2). The Dirac Hamiltonian (2.21) describes $d_{BC}$-dimensional band crossings (with $d_{BC} = d - p$), which are located at

$$\boldsymbol{k} = (0, \ldots, 0, \pm\pi/2, k_{p+1}, \ldots, k_d). \tag{2.22}$$

We observe that the band crossings (2.22) are located away from the high-symmetry points $(0, 0, 0, \ldots, 0)$, $(\pi, 0, 0, \ldots, 0)$, $(0, \pi, 0, \ldots, 0)$, etc. of the BZ. The classification of these band crossings proceeds in a similar way as in Sec. II B. It consists of the following steps:

1. Write down a $d$-dimensional Dirac Hamiltonian $H_D$ of the form Eq. (2.21) with $p = d - d_{BC}$, which satisfies all the considered symmetries. The rank of the gamma matrices in Eq. (2.21) should be large enough, such that all symmetries can be implemented in a nontrivial way, but not larger.

2. Check, whether

   – there exists an additional momentum-independent mass term $\tilde{\Gamma}$, which anticommutes with $H_D$ and which is invariant under all symmetries.

   – there exists an additional momentum-dependent kinetic term $\sin k_p \gamma_p$, which anticommutes with $H_D$ and which respects all symmetries.

   If the answer is *yes* for either of the above two points, then the band crossing can be gapped out. Hence, the band crossing is topologically trivial (entries labelled by "0" in Table I). If the answer is *no* for both of the above points, then the band crossing is topologically stable (entries labelled by "$\mathbb{Z}$" or "$\mathbb{Z}_2$" in Table I).

3. To determine whether there is a single or multiple band crossings protected by the symmetries, consider multiple copies of $H_D$, similar to Eq. (2.11).

Using this approach it was shown that only $\mathbb{Z}$-type invariants can ensure the stability of band-crossings off high-symmetry points [2]. ($\mathbb{Z}_2$-type invariants do not give rise to stable band crossings off high-symmetry points.) To exemplify this, we discuss some specific cases.

#### *1. Semimetal with TRS and PHS (class BDI in $d = 2$)*

First, we consider band crossings in a two-dimensional semimetal with time-reversal symmetry and particle-hole symmetry, corresponding to class BDI in Table I. The semimetal is described by a two-band tight-binding model on the square lattice $\mathcal{H} = \sum_{\boldsymbol{k}} \Psi_{\boldsymbol{k}}^\dagger H_{2D}^{\mathrm{BDI}} \Psi_{\boldsymbol{k}}$, where (cf. Eq. (2.21) with $p = 2$)

$$H_{2D}^{\mathrm{BDI}} = \sin k_x \sigma_y + (1 - \cos k_x - \cos k_y)\sigma_x, \tag{2.23}$$

and $\Psi_{\boldsymbol{k}} = (c_{1\boldsymbol{k}}, c_{2\boldsymbol{k}})^T$. The Bloch bands of Eq. (2.23) are given by

$$E_{\boldsymbol{k}} = \pm\sqrt{(\sin k_x)^2 + (1 - \cos k_x - \cos k_y)^2}. \tag{2.24}$$

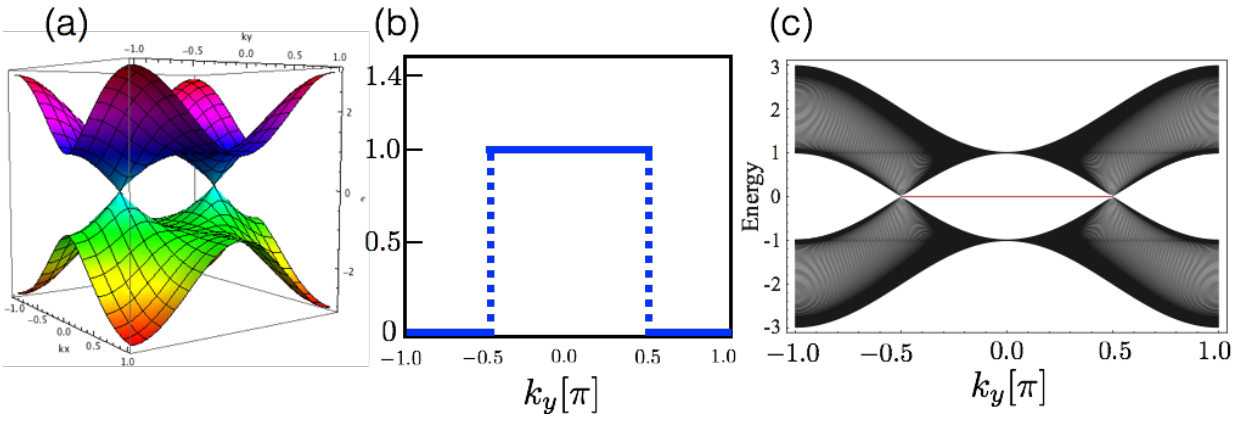


FIG. 3: *Semimetal with TRS and PHS*. (a) Energy spectrum of the semimetal $H_{2D}^{BDI}$, Eq. (2.23). (b) Winding number (2.25) of $H_{2D}^{BDI}$ for contours $\mathcal{L}$ parallel to the $k_x$ direction. (c) Edge spectrum for the (10) edge as a function of edge momentum $k_y$. The flat band edge states are highlighted in red.

At $E = 0$ there are two band crossings ("Dirac points"), which are located at $(0, \pi/2)$ and $(0, -\pi/2)$ in the BZ, see Fig. 3(a). Hamiltonian (2.23) belongs to symmetry class BDI of Table I, since it satisfies both time-reversal symmetry and particle-hole symmetry with $\mathcal{T} = \sigma_0\mathcal{K}$ ($\mathcal{T}^2 = +1$) and $\mathcal{C} = \sigma_z\mathcal{K}$ ($\mathcal{C}^2 = +1$), respectively [cf. Eq. (2.5a)]. We observe that the two band crossings at $\boldsymbol{k} = (0, \pm\pi/2)$ transform into each other under particle-hole and time-reversal symmetry [cf. Fig. 2(b)]. Since the momentum-independent mass term $m\sigma_z$ is forbidden by particle-hole symmetry ($\mathcal{C}^{-1}m\sigma_z\mathcal{C} \neq -m\sigma_z$) and the momentum-dependent kinetic term $\sin k_y\sigma_z$ is forbidden by time-reversal symmetry ($\mathcal{T}^{-1}\sin(-k_y)\sigma_z\mathcal{T} \neq +\sin k_y\sigma_z$), the two band crossings are topologically stable. Furthermore, we find that the band crossings of the doubled version $H_{2D}^{\mathrm{BDI}}\otimes\sigma_0$ are also stable. Therefore, the classification is $\mathbb{Z}$, see second column of Table I.

The stability of these band crossings is guaranteed by a quantized winding number, which takes the form

$$\nu = \frac{1}{2\pi i}\oint_{\mathcal{L}} dk_l\, \partial_{k_l}\left[\ln q(\boldsymbol{k})\right] = \frac{1}{2\pi i}\oint_{\mathcal{L}} dk_l\, \left[q^{-1}(\boldsymbol{k})\partial_{k_l}q(\boldsymbol{k})\right], \tag{2.25}$$

with $q(\boldsymbol{k}) = [(1 - \cos k_x - \cos k_y) - i\sin k_x]/\sqrt{(1 - \cos k_x - \cos k_y)^2 + (\sin k_x)^2}$ and $\mathcal{L}$ is a closed contour in the two-dimensional BZ. The winding number $\nu$, Eq. (2.25), is quantized to $\pm 1$ for closed contours $\mathcal{L}$ encircling one of the two two band crossing points [blue line in Fig. 2(b)], and zero for contours that do not enclose a band crossing [see Fig. 3(b)]. By the bulk-boundary correspondence, a nonzero value of the winding number (2.25) leads to flat-band edge states that connect the two projected band-crossing points in the edge BZ, see Fig. 3(c).

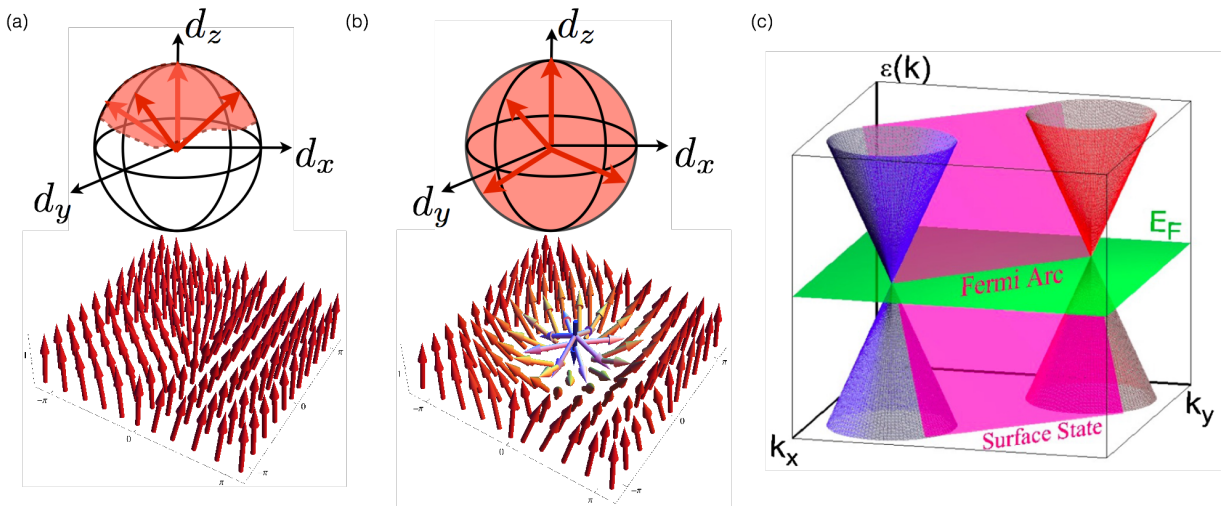


FIG. 4: *Weyl semimetal: Chern number and Fermi arc surface state*. (a),(b) shows the regions covered by the $\boldsymbol{d_k}$-vector, Eq. (2.27), on the unit sphere (upper figures) and the textures of $\boldsymbol{d_k}$ in the two-dimensional contour $\mathcal{C}_{k_z}$ (lower figures). (a) corresponds to $C(k_z) = 0$, while (b) represents $C(k_z) \neq 0$. (c) Fermi arc state at the surface of a Weyl semimetal. Figure taken from Ref. [8].

### 2. *Weyl semimetal (class A in $d = 3$)*

Next, we study the band crossing points of a three-dimensional Weyl semimetal (cf. Sec. II B 2). The Hamiltonian is given by $\mathcal{H}^A_{3D} = \sum_{\boldsymbol{k}} \Psi_{\boldsymbol{k}} H^A_{3D} \Psi_{\boldsymbol{k}}$, with (cf. Eq. (2.21) with $p = 3$)[5]

$$H^A_{3D} = \sin k_x \sigma_x + \sin k_y \sigma_y + (2 - \cos k_x - \cos k_y - \cos k_z)\sigma_z, \tag{2.26}$$

and the spinor $\Psi_{\boldsymbol{k}} = (c_{1\boldsymbol{k}}, c_{2\boldsymbol{k}})$, which has two orbital degrees of freedom (e.g., $s$ and $p$ orbitals), but no spin-degree of freedom, since the semimetal is assumed to be magnetically ordered. The spectrum of Eq. (2.26) is given by $E_{\boldsymbol{k}} = \pm\sqrt{(\sin k_x)^2 + (\sin k_y)^2 + (2 - \cos k_x - \cos k_y - \cos k_z)^2}$. $H^A_{3D}$ exhibits two band crossing points at $E = 0$ (called Weyl points), which are located at $(0, 0, \pm\pi/2)$. As in Sec. II B 2, we find that these Weyl nodes are topologically stable, since there does not exist any any fourth gamma matrix of rank two. (I.e., there exist no additional mass or kinetic terms.) We also find that the doubled version $H^A_{3D} \otimes \sigma_0$ has stable band crossigs. Hence, the classification is of $\mathbb{Z}$ type, see third column of Table I.

[5] Note that this model has an inversion symmetry, i.e., $(\sigma_z)^{-1} H^A_{3D}(-\boldsymbol{k})\sigma_z = H^A_{3D}(\boldsymbol{k})$, wich ensures that the two Weyl points are at the same energy.

The stability of the Weyl points is guaranteed by a quantized Chern number $C = \frac{1}{2\pi} \oint_{\mathcal{C}} \mathcal{F}(\boldsymbol{k}) d\boldsymbol{k}$, where $\mathcal{F}(\boldsymbol{k})$ is the Berry curvature[6] of the occupied band and $\mathcal{C}$ is a two-dimension closed integration contour. The Chern number $C$ is $\pm 1$ for contours $\mathcal{C}$ that enclose one of the two Weyl points, and zero for contours that do not enclose a Weyl point. If we choose $\mathcal{C}$ to be parallel to the $k_x k_y$-plane, the Chern number takes the simple form[7]

$$C(k_z) = \frac{1}{4\pi} \oint_{\mathcal{C}_{k_z}} dk_x dk_y \, \hat{\boldsymbol{d}}_{\boldsymbol{k}} \cdot \left[ \partial_{k_x} \hat{\boldsymbol{d}}_{\boldsymbol{k}} \times \partial_{k_y} \hat{\boldsymbol{d}}_{\boldsymbol{k}} \right], \qquad \text{with} \quad \hat{\boldsymbol{d}}_{\boldsymbol{k}} = \frac{\boldsymbol{d}(\boldsymbol{k})}{|\boldsymbol{d}(\boldsymbol{k})|}, \tag{2.27}$$

and $d_x(\boldsymbol{k}) = \sin k_x$, $d_y(\boldsymbol{k}) = \sin k_y$, and $d_z(\boldsymbol{k}) = (2 - \cos k_x - \cos k_y - \cos k_z)$. The Chern number $C(k_z)$, Eq. (2.27), measures how many times the $\hat{\boldsymbol{d}}_{\boldsymbol{k}}$-vector wraps around the unit sphere $S^2$ as $\boldsymbol{k}$ sweeps through the two-dimensional contour $\mathcal{C}_{k_z}$, see Figs. 4(a) and 4(b). (Note that $\hat{\boldsymbol{d}}_{\boldsymbol{k}}$ defines a map from $\mathcal{C}$ to $S^2$, whose topology is given by the second homotopy group $\pi_2(S^2) = \mathbb{Z}$ [55].) For $|k_z| > \pi/2$ the $\hat{\boldsymbol{d}}_{\boldsymbol{k}}$-vector only covers a small region around the north pole of $S^2$, leading to a zero Chern number $C(k_z) = 0$, see Fig. 4(a). For $-\pi/2 < k_z < +\pi/2$, however, the $\hat{\boldsymbol{d}}_{\boldsymbol{k}}$-vector wraps around the unit sphere $S^2$ once, giving a nonzero Chern number $C(k_z) = 1$, Fig. 4(b). Correspondingly, the $\hat{\boldsymbol{d}}_{\boldsymbol{k}}$-vector exhibits a Skyrmion texture within the contour $\mathcal{C}_{k_z}$, see lower part of Fig. 4(b). By the bulk-boundary correspondence, a nonzero Chern number leads to the appearance of a Fermi arc at the surface, which is located in between the two Weyl points, see Fig. 4(c).

### 3. *Dirac nodal-line semimetal (class AI + R in $d = 3$)*

As a third example, we study a nodal-line band crossing in a three-dimensional semimetal with time-reversal symmetry (class AI) and reflection symmetry [12, 15]. The Hamiltonian is defined on the cubic lattice and is given by $\mathcal{H}_{3D}^{AI+R} = \sum_{\boldsymbol{k}} \Psi_{\boldsymbol{k}}^\dagger H_{3D}^{AI+R} \Psi_{\boldsymbol{k}}$, where the spinor $\Psi_{\boldsymbol{k}} = (c_{p\boldsymbol{k}}, c_{d\boldsymbol{k}})^T$ describes spinless Bloch electrons (no spin-orbit coupling) originating from $p$ and $d$ orbitals and

[6] The Berry curvature is defined as $\mathcal{F}(\boldsymbol{k}) = \nabla_{\boldsymbol{k}} \times \boldsymbol{A}_{\boldsymbol{k}}$, where $\boldsymbol{A}_{\boldsymbol{k}} = i\langle u_-(\boldsymbol{k}) | \nabla_{\boldsymbol{k}} | u_-(\boldsymbol{k}) \rangle$ is the Berry connection and $|u_-(\boldsymbol{k})\rangle$ is the Bloch state of the occupied band.

[7] The fact that there is a non-zero Chern number can also be diagnosed from the parity eigenvalues at the TRIMs [5, 54]. The parity eigenvalues at the $\Gamma$ point are opposite to those at all the other TRIMs. From this it follows that the Chern number $C(k_z = 0)$ must be non-zero.

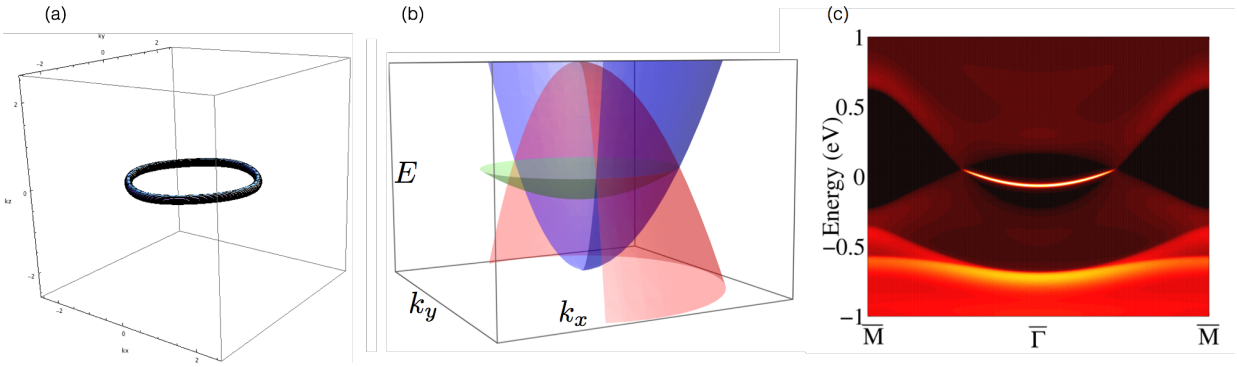


FIG. 5: *Dirac nodal-line semimetal.* (a) The spectrum of Hamiltonian (2.28) exhibits a band crossing along a nodal loop. (b), (c) Drumhead surface state of the Hamiltonian (2.28). Taken from Ref. [12].

$H_{3D}^{AI+R}$ reads (cf. Eq. (2.21) with $p = 2$)[8]

$$H_{3D}^{AI+R} = \sin k_z \sigma_2 + [2 - \cos k_x - \cos k_y - \cos k_z]\, \sigma_3. \tag{2.28}$$

The spectrum of this Hamiltonian

$$E_{\boldsymbol{k}} = \pm\lambda = \pm\sqrt{(2 - \cos k_x - \cos k_y - \cos k_z)^2 + (\sin k_z)^2}, \tag{2.29}$$

exhibits a band-crossing at $E = 0$, which is located along a nodal ring within the $k_z = 0$ plane, see Fig. 5(a). Such a nodal-line band crossing at the Fermi energy is realized in $Ca_3P_2$ [12, 26], CaAgP [27] and other materials. Eq. (2.28) is time-reversal symmetric with the time-reversal operator $\mathcal{T} = \sigma_0\mathcal{K}$, and reflection symmetric, $R^{-1}H_{3D}^{AI+R}(k_x, k_y, -k_z)R = H_{3D}^{AI+R}(k_x, k_y, k_z)$, with the reflection operator $R = \sigma_z$. There is also an inversion symmetry, $\mathcal{P}^{-1}H_{3D}^{AI+R}(-\boldsymbol{k})\mathcal{P} = H_{3D}^{AI+R}(\boldsymbol{k})$, with the inversion operator $\mathcal{P} = \sigma_z$. We observe that the only possible mass term $m\tau_x$, which anticommutes with $H_{3D}^{AI+R}$, is symmetry forbidden, since it breaks reflection symmetry ($R^{-1}m\sigma_x R = -m\sigma_x$) and space-time inversion symmetry [ $(\mathcal{TP})^{-1}m\sigma_x(\mathcal{TP}) = -m\sigma_x$]. Hence, the nodal line band crossing is stable and protected by reflection symmetry and $\mathcal{PT}$ symmetry. However, the band crossing of the doubled version of $H_{3D}^{AI+R}$

$$H_{3D}^{AI+R,\mathrm{db}} = \sin k_z \sigma_2 \otimes \sigma_0 + [2 - \cos k_x - \cos k_y - \cos k_z]\, \sigma_3 \otimes \sigma_0. \tag{2.30}$$

[8] Here, we have included both $\cos k_x$ and $\cos k_y$ terms in order to deform the nodal line of Eq. (2.21) into a nodal ring.

is protected only by reflection symmetry but not by $\mathcal{PT}$ symmetry, since the mass term $\hat{m} = \sigma_x \otimes \sigma_y$ is symmetric under $\mathcal{PT}$ [$(\sigma_z \otimes \sigma_0 \mathcal{K})^{-1} \hat{m} (\sigma_z \otimes \sigma_0 \mathcal{K}) = \hat{m}$], but breaks $R$ [$(\sigma_z \otimes \sigma_0)^{-1} \hat{m} (\sigma_z \otimes \sigma_0) \neq \hat{m}$]. From this we conclude that nodal rings of type (2.28) have a $\mathbb{Z}$ classification in the presence of reflection symmetry, but only a $\mathbb{Z}_2$ classification in the presence of $\mathcal{PT}$ symmetry.

The topological invariant, which guarantees the stability of the nodal ring, is the Berry phase, which is defined as a one-dimensional contour integral over the Berry connection [9]

$$P_{\mathcal{L}} = -i \oint_{\mathcal{L}} dk_l \, \langle u_-(\boldsymbol{k}) | \, \nabla_{k_l} \, | u_-(\boldsymbol{k}) \rangle \, . \tag{2.31}$$

Here, $|u_-(\boldsymbol{k})\rangle$ is the filled Bloch eigenstate of Eq. (2.28), which is given by

$$|u_-(\boldsymbol{k})\rangle = \frac{1}{\sqrt{2\lambda(\lambda - M_{\boldsymbol{k}})}} \begin{pmatrix} \lambda - M_{\boldsymbol{k}} \\ i \sin k_z \end{pmatrix} \tag{2.32}$$

with $M_{\boldsymbol{k}} = 2 - \cos k_x - \cos k_y - \cos k_z$. Note that the Berry phase is only defined up to mod $2\pi$. One can show that reflection symmetry $R$ and space-time inversion $\mathcal{PT}$ lead to the quantization of the Berry phase, i.e., $P_{\mathcal{L}} \in \{0, \pi\}$ [12]. To numerically compute the Berry phase, it is advantageous to use an alternative definition of the Berry phase, in terms of the Wilson loop [56–58], see Appendix C. The Berry phase evaluates to $\pm\pi$ for any contour $\mathcal{L}$ that interlinks with the nodal-line band crossing; and it is zero for any contour that does not interlink with the nodal-line band crossing. By the bulk-boundary correspondence, a nonzero Berry phase $P_{\mathcal{L}}$ leads to the appearance of of a drumhead surface state, which spans the region inside the projected nodal line in the surface BZ, see Figs. 5(b) and 5(c).

#### 4. *Spin-triplet superconductor (class DIII + $R_{--}$ in $d = 3$)*

As the last example of this section, we study point band crossings in a three-dimensional reflection and time-reversal symmetric superconductor with spin-orbit coupling and spin-triplet pairing. The Hamiltonian $\mathcal{H}_{3D}^{DIII+R} = \sum_{\boldsymbol{k}} \Psi_{\boldsymbol{k}}^\dagger h_{3D}^{DIII+R} \Psi_{\boldsymbol{k}}$ is defined in terms of the Nambu spinor $\Psi_{\boldsymbol{k}} = (c_{\uparrow,\boldsymbol{k}}^\dagger, c_{\downarrow,\boldsymbol{k}}^\dagger, c_{\uparrow,-\boldsymbol{k}}, c_{\downarrow,-\boldsymbol{k}})^T$ and (cf. Eq. (2.21) with $p = 3$)

$$h_{3D}^{DIII+R} = \sin k_x \sigma_x \otimes \sigma_x + \sin k_z \sigma_x \otimes \sigma_z + M(\boldsymbol{k}) \sigma_z \otimes \mathbb{1} \tag{2.33}$$

with the momentum-dependent mass therm $M(\boldsymbol{k}) = 2.5 - \cos k_x - \cos k_y - \cos k_z$. The Bogoliubov quasiparticle spectrum of this Hamiltonian exhibits a band crossing (i.e., a node) at the two

[9] There is also a mirror invariant, see Ref. [12].

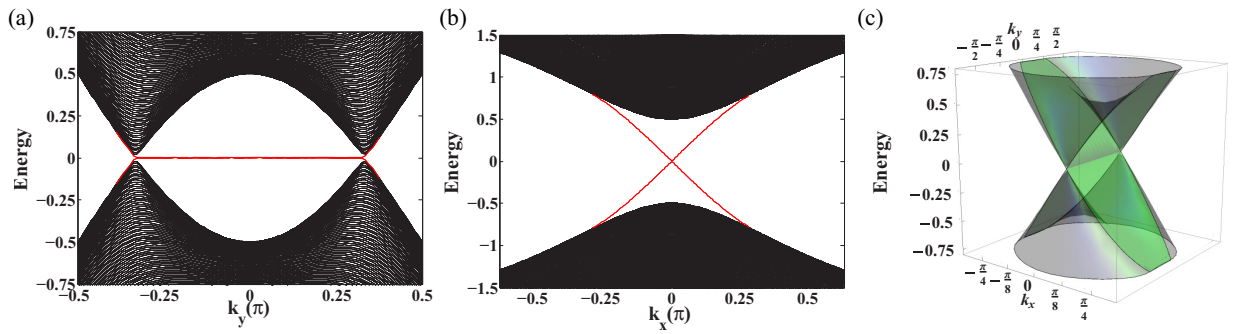


FIG. 6: *Surface states of spin-triplet superconductor.* Majorana arc states at the (001) surface of the spin-triplet superconductor (2.33). (a), (b) show the Majorana arcs as a function of surface momentum $k_y$ and $k_x$, respectively. (c) shows the Majorana arc (green shaded area) as a function of both $k_x$ and $k_y$. Taken form Ref. [19].

points $\boldsymbol{k} = (0, \pm\pi/3, 0)$. Hamiltonian (2.33) satisfies time-reversal symmetry and particle-hole symmetry with $\mathcal{T} = \mathbb{1} \otimes \sigma_y \mathcal{K}$ and $\mathcal{C} = \sigma_x \otimes \mathbb{1}\mathcal{K}$, respectively, and is reflection symmetric under $k_x \to -k_x$ with $R = \sigma_z \otimes \sigma_x$. Because $\mathcal{T}^2 = -1$, $\mathcal{C}^2 = +1$, $\{\mathcal{T}, R\} = 0$, and $\{\mathcal{C}, R\} = 0$, Eq. (2.33) is classified as DIII with $R_{--}$, according to the nomenclature of Refs. [19, 47]. The two band-crossing points, which are located within the mirror plane $k_x = 0$, are protected by time-reversal, particle-hole, and reflection symmetry, since there does not exist any additional symmetry-preserving masst term or kinetic term. We note that the gap opening term $\sin k_y \sigma_y \otimes \mathbb{1}$ is symmetric under time-reversal and particle-hole symmetry, but breaks reflection symmetry, which shows that the reflection symmetry $R$ is crucial for the protection of the band-crossing point. Indeed, as indicated by the entry in the third column of Table I, the band-crossing points are unstable in the absence of reflection symmetry.

The stability of this band-crossing point is guaranteed by a mirror winding number. This mirror winding number is defined in terms of an integral along a one-dimensional closed contour, which is located within the mirror plane $k_x = 0$. In order to define this mirror invariant, we first need to block diagonalize $h_{3D}^{DIII+R}$ with respect to $R$. Each of the two blocks is symmetric under the chiral symmetry (2.5b) with $\mathcal{S} = \mathcal{T}\mathcal{C} = \sigma_x \otimes \sigma_y$, since $\mathcal{S}$ commutes with $R$. This allows us to define a winding number for each block separately, which for the $R = +1$ eigenspace takes the form of Eq. (2.25) with

$$q(\boldsymbol{k}) = \frac{M(\boldsymbol{k}) - i \sin k_z}{\sqrt{M(\boldsymbol{k})^2 + (\sin k_z)^2}}. \tag{2.34}$$

Choosing the contour $\mathcal{L}$ along the $k_z$ axis with $k_x = 0$ and $k_y$ a fixed parameter, we find that the mirror winding number evaluates to

$$n^{+}_{M\mathbb{Z}}(k_y) = \begin{cases} 1, & 0 \leq |k_y| < \frac{\pi}{3} \\ 0, & \frac{\pi}{3} < |k_y| \leq \pi \end{cases} . \tag{2.35}$$

By the bulk boundary correspondence, the nontrivial value of Eq. (2.35) leads to zero-energy arc states (Majorana arc states) on surfaces that are perpendicular to the mirror plane. As shown in Fig. 6, these zero-energy Majorana arcs connect two projected point nodes in the surface BZ.

## III. SYMMETRY-ENFORCED BAND CROSSINGS

In this section we study symmetry-enforced band crossings that are *movable* (but not removable) [16, 33, 34, 36–39, 59]. Note that there are also symmetry-enforced band crossings which are not movable, since they are pinned at a particular high-symmetry point (or line) of the BZ. These non-movable band crossings arise, for example, when all possible irreps at a point of the BZ have dimension larger than one. A classic example of these non-movable band crossings are Kramers degeneracies at time-reversal invariant points (e.g., the $\Gamma$ point). Here, however, we focus on symmetry-enforced band crossings which are movable.

These movable band crossings, which are required to exist by symmetry alone, exhibit the following properties:

- They are protected by nonsymmorphic crystal symmetries, possibly together with nonspatial symmetries. A nonsymmorphic symmetry is a symmetry $G = \{g, \boldsymbol{t}\}$, which combines a point-group symmetry $g$ with a translation $\boldsymbol{t}$ by a fraction of a Bravais lattice vector (see Sec. III A).

- Symmetry-enforced band crossings are characterized by a global topological charge, which

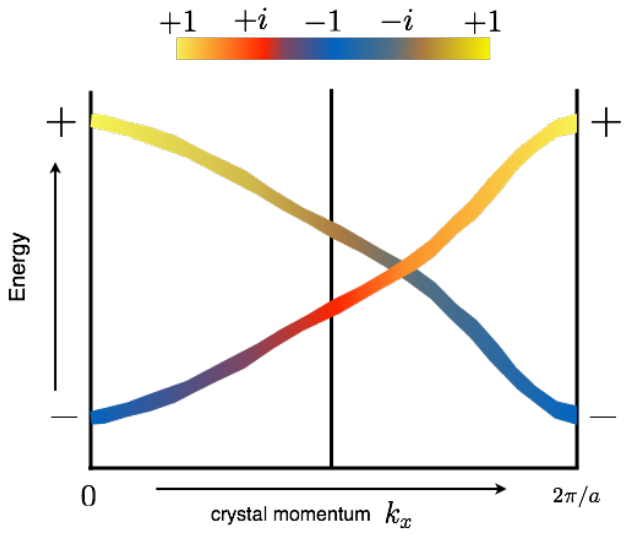


FIG. 7: *Symmetry-enforced band crossings*. Nonsymmorphic symmetries lead to symmetry-enforced band crossings. The color shading indicates how the eigenvalue of the nonsymmorphic symmetry changes as a function of the crystal momentum. Note that one needs to go through the BZ twice (or $n$ times), in order to get back to the same eigenvalue.

measures the winding of the eigenvalue of $G$ as we go through the BZ. As shown in Fig. 7, one needs to go twice (or $n$ times) through the BZ in order to get back to the same eigenvalue.

- Symmetry-enforced band crossings are globally stable. That is, they cannot be removed, even by large symmetry-preserving deformations. They are required to exist by symmetry alone, independent of any other material details (e.g, chemical composition or energetics of the bands).

#### *1. Strategy for materials discovery*

The last point above allows us to construct the following strategy to discover new materials with topological band crossings [42], which consists of three steps:

(i) First, we identify the space groups (SGs) whose nonsymmorphic symmetries enforce the desired band crossings. This can be done by either (i) computing the algebraic relations obeyed by the symmetry operators or (ii) by computing the compatibility relations between irreducible symmetry representations (irreps).

(ii) Second, we perform a database search for materials in these SGs. The most comprehensive database on inorganic crystals is the Inorganic Crystal Structure Database (ICSD) from the Leibniz Institute in Karlsruhe [60]. Other databases, which also contain calculated band structures, are the AFLOW database [61], the Materials Project database [62, 63], and the database for material sciences at the Institute of Physics of the Chinese Academy of Science [64].

(iii) Third, we compute the electronic band structure of these materials to check whether the band crossings are near the Fermi energy.

In Sec. III B we will apply this strategy to discover new topological semimetals with hexagonal symmetries.

### A. Basic mechanism of symmetry enforcement

Nonsymmorphic symmetries $G = \{g|\boldsymbol{t}\}$ combine a point-group symmetry $g$ with a translation $\boldsymbol{t}$ by a fraction of a Bravais lattice vector, see Fig. 8. The fractional translation $\boldsymbol{t}$ can be assumed to

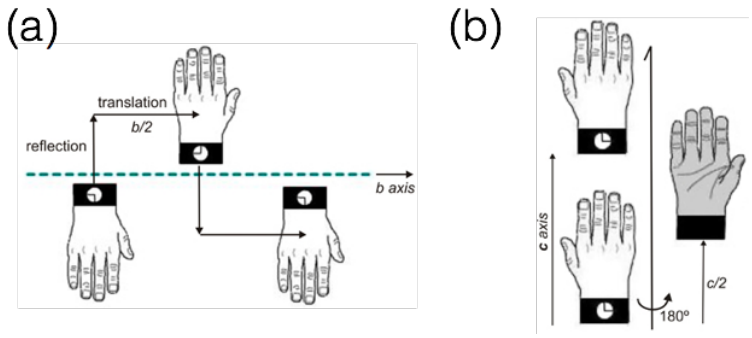


FIG. 8: *Nonsymmorphic symmetries*. This figure illustrates two nonsymmorphic symmetries: A glide reflection in panel (a) and a two-fold screw rotation in panel (b).

satisfy $g\boldsymbol{t} = \boldsymbol{t}$, i.e., $\boldsymbol{t}$ is parallel to the invariant space of $g$. This is because any component of $\boldsymbol{t}$ that is not invariant under $g$ can be removed by a suitable choice of reference of $g$ (suitable choice of unit cell). (An exception to this rule will be discussed in Sec. III B 3.) Applying an $n$-fold nonsymmorphic symmetry $n$ times yields an element of the lattice translation group, i.e.,

$$G^n = \{g^n|n\boldsymbol{t}\} = \pm p\, T_{\boldsymbol{a}}, \quad p \in \{1, 2, \ldots, n-1\}, \tag{3.1}$$

where $g$ is an $n$-fold point-group symmetry and $T_{\boldsymbol{a}}$ is the translation operator for the Bravais lattice vector $\boldsymbol{a}$. The $\pm$ sign on the right-hand side of Eq. (3.1) originates from $g^n$, which equals $-1$ for spin-1/2 quasiparticles (Bloch electrons with spin-orbit coupling) and $+1$ for spinless quasiparticles (Bloch electrons without spin-orbit coupling). Two simple examples of nonsymmorphic symmetries are illustrated in Fig. 8:

- a glide reflection $M = \{m|\boldsymbol{t}\}$, with $M^2 = \pm T_{\boldsymbol{a}}$
- a two-fold screw rotation $C_2 = \{c_n|\boldsymbol{t}\}$, with $(C_2)^2 = \pm T_{\boldsymbol{a}}$

In the band structure of materials with nonsymmorphic symmetries, the operators $G = \{g|\boldsymbol{t}\}$ can lead to the protection of band degeneracies in the $g$-invariant space of the BZ, which satisfies $g\boldsymbol{k} = \boldsymbol{k}$. In these $g$-invariant lines and planes of the BZ, the Bloch states $|u_m(\boldsymbol{k})\rangle$ can be constructed in such a way that they are simultaneous eigenfunctions of both $G$ and the Hamiltonian. From Eq. (3.1) it follows that in momentum space $G^n$ is

$$G^n = \pm e^{-ip\boldsymbol{k}\cdot\boldsymbol{a}}. \tag{3.2}$$

Hence, the eigenvalues of $G$ are

$$G\left|\psi_m(\boldsymbol{k})\right\rangle = \begin{cases} e^{i\pi(2m+1)/n} e^{-ip\boldsymbol{k}\cdot\boldsymbol{a}/n}\left|\psi_m(\boldsymbol{k})\right\rangle, & \text{for spin 1/2,} \\ e^{i2\pi m/n} e^{-ip\boldsymbol{k}\cdot\boldsymbol{a}/n}\left|\psi_m(\boldsymbol{k})\right\rangle, & \text{for spin 0,} \end{cases} \tag{3.3}$$

where $m \in \{0, 1, \ldots, n-1\}$. Due to the momentum dependent phase factor $e^{-ip\boldsymbol{k}\cdot\boldsymbol{a}/n}$ in Eq. (3.3) the eigensectors of $G$ can be interchanged, as $\boldsymbol{k}$ is moved across the $g$-invariant space of the BZ. As a consequence, provided there are no additional degeneracies due to other symmetries, pairs of bands must cross at least once within the invariant space. This is the basic mechanism that leads to the protection of band degeneracies [16, 33, 35–38],

Let us now explain in more detail how a screw rotation leads to a symmetry-enforced band crossing in a simple one-dimensional system with two atoms per unit cell. In momentum space such a system is described by a two-band Hamiltonian $\mathcal{H}(k)$. The screw rotation symmetry ($\pi$ rotation, followed by half translation) takes the form [33]

$$G(k)\mathcal{H}(k)G^{-1}(k) = \mathcal{H}(k), \qquad G(k) = \begin{pmatrix} 0 & e^{-ik} \\ 1 & 0 \end{pmatrix}, \tag{3.4}$$

where the exponential factor $e^{-ik}$ accounts for the fact that one of the two atoms is moved to the next unit cell. Here, we consider the case of spin-0 quasiparticles (Bloch electrons without spin-orbit coupling), hence $G(k)$ does not contain a spin part. Now, since $G^2(k) = \sigma_0 e^{-ik}$ the eigenvalues of $G$ are $\pm e^{-ik/2}$, i.e., we can label the two bands of $H(k)$ by the eigenvalues of $G(k)$

$$G\left|\psi_\pm(\boldsymbol{k})\right\rangle = \pm e^{-ik/2}\left|\psi_\pm(\boldsymbol{k})\right\rangle, \tag{3.5}$$

cf. Eq. (3.3) with $n = 2$ and $p = 1$. We see that the eigenvalues are momentum dependent and change from $\pm$ at $k = 0$ to $\mp$ at $k = 2\pi$, as we go through the BZ. Hence, the two eigenspaces get interchanged and the bands must cross at least once, see Fig. 7.

It is also possible to mathematically prove that there needs to be at least one crossing [33]. The proof is by contradiction. First, we observe that $G(k)$ does not commute with $\sigma_3$ (it anti-commutes). Therefore, $\mathcal{H}(k)$ cannot contain a term proportional to $\sigma_3$, since it is symmetry forbidden. Moreover, we can drop terms proportional to the identity, since they only shift the energy of the eigenstates, but do not alter the band crossings. For this reason the Hamiltonian can be assumed to be off-diagonal and can be written as

$$H(k) = \begin{pmatrix} 0 & q(k) \\ q^*(k) & 0 \end{pmatrix}. \tag{3.6}$$

With this parametrization, the spectrum of $\mathcal{H}(k)$ is symmetric around $E = 0$ and is given by $E = \pm|q(k)|$. For this reason, any band crossing must occur at $E = 0$. Applying the symmetry constraint (3.4), we find that $q(k)$ must satisfy

$$q(k)e^{ik} = q^*(k). \tag{3.7}$$

We now need to show that any periodic function $q(k)$ satisfying the constraint (3.7) must have zeros, corresponding to a band crossing point. To see this, we introduce the complex variable $z := e^{ik}$ and the complex function $f(z) := q(k)$. From Eq. (3.7) it follows that $zf(z) = f^*(z)$. Assuming that $f(z)$ is nonzero on the unit circle $S^1$, then

$$z = f^*(z)/f(z), \tag{3.8}$$

which, however, leads to a contradiction. This is because for $z \in S^1$ the two sides of Eq. (3.8) both define functions from $S^1$ to $S^1$. But the left hand side has winding number 1, while the right hand side has *even* winding number, since $f^*(z)/f(z) = e^{2i\mathrm{Arc}[f(z)]}$. Thus, $f(z)$ and $q(k)$ must vanish at some $k$ by contradiction. Therefore, there most be a band crossing point somewhere in the BZ.

Note that a similar proof can be constructed also for multiband systems with chiral symmetry. Hamiltonians with chiral symmetry can be anti-diagonalized with the upper-right block being a matrix $\Delta(k)$. One can then show that $\mathrm{Det}[\Delta(k)]e^{ik} = (\mathrm{Det}[\Delta(k)])^*$, similar to Eq. (3.7). The argument given around Eq. (3.8) then implies that $\mathrm{Det}[\Delta(k)]$ has to vanish somewhere in the BZ. Hence, there must be a zero in the spectrum which corresponds to a band crossing.

### B. Examples of symmetry-enforced band crossings

We now discuss more complicated examples of three-dimensional systems with nonsymmorphic symmetries and time-reversal symmetry. For concreteness, we consider hexagonal systems with spin-orbit coupling, as they show a rich variety of nonsymmorphic band crossings [42]. Using the strategy of Sec. III 1, we search for new topological semimetals with hexagonal symmetry.

#### *1. Weyl lines protected by glide reflection*

Let us first study Weyl nodal lines wich occur in the hexagonal SG $P\bar{6}2c$ (No. 190). This SG contains a glide reflection symmetry of the form

$$M_x \ : \ (x, y, z) \to (-x, y, z + \tfrac{1}{2})i\sigma_x, \tag{3.9}$$

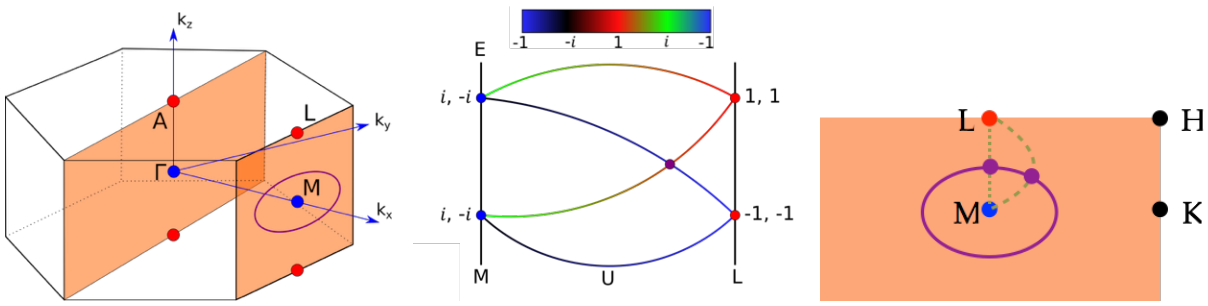


(a) (b) (c)

FIG. 9: *Weyl nodal line with hourglass dispersion.* (a) Weyl nodal line in the $k_x = \pi$ plane protected by the glide mirror symmetry $M_x$, Eq. (3.9). (b) Band connectivity diagram for a line connecting M and L within the $k_x = \pi$ plane, which is left invariant by $M_x$. The bands are Kramers degenerate at M and L. The color shading indicates the $M_x$ eigenvalues (3.10) of the Bloch bands. (c) The Bloch bands along any path within the $k_x = \pi$ plane, connecting M to L, exhibit the band connectivity shown in (b).

where the Pauli matrix $\sigma_x$ operates in spin space. Here we consider spin-1/2 quasiparticles, i.e., Bloch electrons with spin-orbit coupling. Applying this glide reflection twice yields minus a unit translation in the x direction, i.e., $-\hat{T}_x$, where the minus sign is due to the spin part. The glide reflection (3.9) leaves two planes in the BZ invariant, namely the $k_x = 0$ plane and the $k_x = \pi$ plane, see Fig. 9(a).

*a. Symmetry eigenvalues.* Within the invariant planes $k_x = 0$ and $k_x = \pi$, the Boch bands can be chosen to be eigenstates of the glide mirror operator $M_x$ with the eigenvalues

$$M_x \left|\psi_\pm(\boldsymbol{k})\right\rangle = \pm i e^{-ik_z/2} \left|\psi_\pm(\boldsymbol{k})\right\rangle , \tag{3.10}$$

which follows from Eq. (3.3) with $p = 1$ and $n = 2$.

Next, we add time-reversal symmetry to the game, since we want to study nonmagnetic systems. Time-reversal symmetry sends the crystal momentum $\boldsymbol{k}$ to $-\boldsymbol{k}$ and acts on the Hamiltonian as

$$\mathcal{T}^{-1} H(-\boldsymbol{k}) \mathcal{T} = +H(\boldsymbol{k}), \tag{3.11}$$

with the operator $\mathcal{T} = i\sigma_y \mathcal{K}$ and $\mathcal{K}$ the complex conjugation operator. Time-reversal symmetry leaves two points in the $k_x = 0$ and $k_x = \pi$ planes invariant, see blue and red dots in Fig. 9(a). These points are called time-reversal invariant momenta (TRIMs). Due to spin-orbit coupling, the energy bands $|\psi_m(\boldsymbol{k})\rangle$ are in general non-degenerate, except at the TRIMs, where time-reversal symmetry enforces twofold degeneracies, due to Kramers theorem (Appendix A). Since $\mathcal{T}$ contains

the complex conjugation operator $\mathcal{K}$, time-reversal symmetry pairs up bands whose $M_x$ eigenvalues are complex conjugate pairs. It follows from Eq. (3.10) that at the L point of the $k_x = \pi$ plane the $M_x$ eigenvalues are $+1$ and $-1$, while at the M point they are $+i$ and $-i$. (Similar arguments hold for the TRIMs in the $k_x = 0$ plane.) Hence, at M time-reversal symmetry enforces Kramers degeneracies between pairs with opposite $M_x$ eigenvalues [blue dot in Fig. 9(a)], while at L Kramers pairs are formed between bands with the same $M_x$ eigenvalues [red dot in Fig. 9(a)]. This is shown in Fig. 9(b), where the $M_x$ eigenvalues are indicated by the color shading. We see that since the Kramers pairs switch partners as we go from M to L, the bands most cross at least once forming a group of four connected bands with an *hourglass dispersion*. Because this holds for any one-dimensional path within the $k_x = \pi$ plane, connecting M to L, the $k_x = \pi$ plane must contain a Weyl line degeneracy, as shown in Fig. 9(c).

*b. Compatibility relations.* The symmetry-enforced Weyl nodal lines of SG 190 ($P\bar{6}2c$) can also be derived from the compatibility relations between irreducible representations (irreps) at different high-symmetry points (or lines) of the BZ [65, 66]. In order to explain how this is done we first need to review some basic facts about double SGs and their irreps [67].

The symmetries of band sructures with spin-orbit coupling and time-reversal symmetry (i.e., with a $\mathcal{T}$ operator that squares to $-1$) are described by *double crystallographic SGs* and their *double-valued irreducible representations* [66, 67]. If we restrict the total band structure to a particular high-symmetry point $\boldsymbol{k}$ (or high-symmetry line) in the BZ, then the symmetries of the band structure are reduced to a subgroup of the double SG, which is called the little group at $\boldsymbol{k}$, $\mathcal{G}_{\boldsymbol{k}}$. Since the Hamiltonian restricted to $\boldsymbol{k}$ commutes with the corresponding little group $\mathcal{G}_{\boldsymbol{k}}$, we can label its Bloch bands by the double valued irreps of the little group $\overline{\boldsymbol{D}}_{\boldsymbol{k}}$. Moving in a continuous way from a point with high symmetry ($\boldsymbol{k}_1$, say) to a point with lower symmetry ($\boldsymbol{k}_2$, say), we find that the little-group irreps at these two points must be related to each other, as the little groups at $\boldsymbol{k}_1$, $\mathcal{G}_{\boldsymbol{k}_1}$, and $\boldsymbol{k}_2$, $\mathcal{G}_{\boldsymbol{k}_2}$, form a group-subgroup pair, $\mathcal{G}_{\boldsymbol{k}_2} \subset \mathcal{G}_{\boldsymbol{k}_1}$ . In fact, a representation of the little group at $\boldsymbol{k}_2$ can be subduced from the little-group irreps at $\boldsymbol{k}_1$

$$\overline{\boldsymbol{D}}_{\boldsymbol{k}_1} \downarrow \mathcal{G}_{\boldsymbol{k}_2} = \overline{\boldsymbol{D}}_{\boldsymbol{k}_2}. \tag{3.12}$$

By decomposing this subduced representation $\overline{\boldsymbol{D}}_{\boldsymbol{k}_2}$ into irreps, one obtains the compatibility relations between the irreps at $\boldsymbol{k}_1$ and $\boldsymbol{k}_2$ [66, 68]. These compatibility relations then determine the connectivity of the Bloch bands in the BZ.

We will now show how this works for SG 190. To determine the connectivity between the bands

| Irrep\Element | E | $M_x$ |
|---|---|---|
| $\overline{M}_5$ | $\begin{pmatrix} +1 & 0 \\ 0 & +1 \end{pmatrix}$ | $\begin{pmatrix} +i & 0 \\ 0 & -i \end{pmatrix}$ |
| $\overline{L}_2$ | $+1$ | $-1$ |
| $\overline{L}_3$ | $+1$ | $-1$ |
| $\overline{L}_4$ | $+1$ | $+1$ |
| $\overline{L}_5$ | $+1$ | $+1$ |
| $\overline{C}'_3$ | $+1$ | $e^{\frac{i}{2}(\pi+k_z)}$ |
| $\overline{C}'_4$ | $+1$ | $e^{-\frac{i}{2}(\pi-k_z)}$ |

TABLE II: Double valued irreps of SG 190 ($P\bar{6}2c$) at the TRIMs M and L and within the mirror plane $k_z = \pi$, denoted by $C'$. The irreps for $C'$ have momentum-dependent phases due to the partial translation of the glide reflection $M_x$. Here, we use the same convention as in Ref. 66 for the labelling of the irreps.

we first need to determine the little group irreps at the TRIMs M and L, and within the mirror plane $k_x = \pi$, which is denoted by $C'$. Table II lists the double-valued irreps without time-reversal. We find that at the M point there is only one double-valued irrep, namely $\overline{M}_5$, which is two-dimensional and pseudoreal. At the L point there are four different irreps: $\overline{L}_2$, $\overline{L}_3$, $\overline{L}_4$, and $\overline{L}_5$, which are one-dimensional and complex. The irreps for $C'$ are all one-dimensional and have $\boldsymbol{k}$-dependent phases due to the partial translation of the glide reflection $M_x$, Eq. (3.9). At the TRIMs M and L we need to construct time-reversal symmetric irreps (i.e., real irreps) using Table II. Pseudoreal irreps are time-reversal symmetric by themselves, whereas complex irreps need to be paired up into complex-conjugate pairs to form time-reversal symmetric irreps [67, 68]. Hence, at the L point we need to pair $\overline{L}_2$ with $\overline{L}_3$ and $\overline{L}_4$ with $\overline{L}_5$, see Fig. 10(a). In agreement with Kramers theorem, all time-reversal symmetric irreps at M and L are two-dimensional, leading to two-fold degeneracies. These two-dimensional irreps decompose into one-dimensional irreps as we move from a TRIM to a point within the mirror plane. The compatibility relations tell us how this occurs.

As a next step, we therefore need to derive the compatibility relations between the little-group irreps at M and L, and $C'$. This can be achieved by using the following relation between the

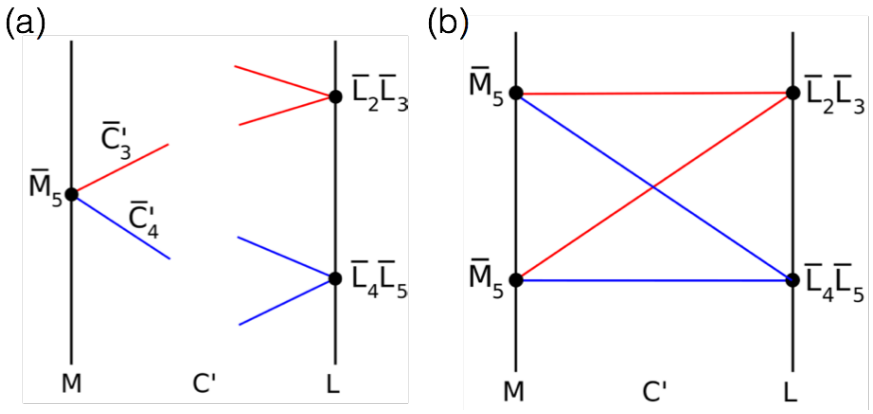


FIG. 10: (a) Compatibility relations for SG 190 between the little-group irreps at M, L and C' ($k_x = \pi$ plane). (b) Band connectivity diagram for SG 190 for a path within the $k_x = \pi$ plane connecting M to L.

characters $\chi$ of the little groups[10]

$$\chi[\overline{D}_l(g)] = \sum_{i=1}^{2} \chi[\overline{C}'_{m_i}(g)], \tag{3.13}$$

where $\chi[\overline{D}_l(g)]$ is the character of the symmetry element $g$ for the time-reversal symmetric irrep $\overline{D}_l$ and $\{\overline{C}'_{m_1}, \overline{C}'_{m_2}\}$ is the set of irreps that $\overline{D}_l$ decomposes into. Eq. (3.13) follows from the fact that the characters of each symmetry must be preserved, as we continuously move from M (or L) to a point on the $C'$ plane. Using Eq. (3.13) we find that the time-reversal symmetric irrep at M (where $k_z = 0$) must decompose into

$$\overline{M}_5 \rightarrow \overline{C}'_3 + \overline{C}'_4, \tag{3.14}$$

while for the real irreps at L (where $k_z = \pi$) we have

$$\begin{aligned} \overline{L}_2\overline{L}_3 &\rightarrow \overline{C}'_3 + \overline{C}'_3, \\ \overline{L}_4\overline{L}_5 &\rightarrow \overline{C}'_4 + \overline{C}'_4. \end{aligned} \tag{3.15}$$

These two sets of equations are the compatibility relations between the little-group irreps at M, L, and $C'$.

The Bloch bands for any path within the $C'$ plane connecting M to L must satisfy all of these compatibility relations. That is, as we move from M to a point within the mirror plane $C'$, Kramers

[10] The character of a group irrep associates with each group element the trace of the corresponding irrep matrix.

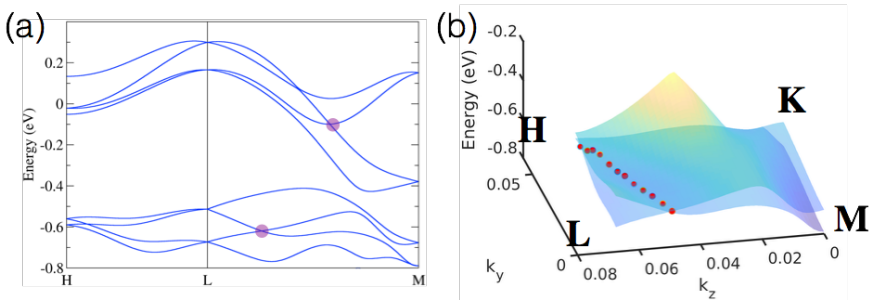


FIG. 11: *Band structure of ZrIrSn.* (a) Electronic band structure of ZrIrSn [42]. The band crossings along the M – L path are part of Weyl nodal lines. (b) The Weyl nodal line at $E \simeq -0.64$ encloses the L point.

pairs must decompose according to Eq. (3.14), while, as we approach L, they must pair up according to Eq. (3.15). As a consequence, the little-group irreps switch partners, as shown in Fig. 10(b). That is, the bands connect in a nontrivial way, with at least one crossing. This is in full agreement with Sec. III B 1 a, cf. Fig. 9(b).

*c. Example material.* We now look for example materials, using the strategy of Sec. III 1. From the above discussion, it follows that any material crystallizing in SG 190 with strong spin-orbit coupling exhibits Weyl nodal lines within the $k_x = \pi$ plane. Hence, to find example materials, we look for compounds with SG 190 in the ICSD database [60]. Focusing on binary or ternary compounds with heavy elements (indicating large spin-orbit coupling), we find the compound ZrIrSn [42]. Its band structure is presented in Fig. 11(a). Along the M – L line, which is invariant under the glide reflection $M_x$, we observe groups of four connected bands, which cross each other at least once. These crossings are part of Weyl nodal lines within the $k_x = \pi$ plane, which enclose the L points, see Fig. 11(b). The topological properties of these Weyl nodal lines are characterized by a nonzero Berry phase [12], which, by the bulk-boundary correspondence, leads to drumhead states at the surface of ZrIrSn. Moreover, due to the absence of inversion, the bands in ZrIrSn carry a nonzero Berry curvature, which is particularly large close to the Weyl nodal lines. In slightly doped samples of ZrIrSn this should give rise to anomalous transport properties, such as, e.g., large anomalous Hall effects or anomalous magnetoelectric responses [16].

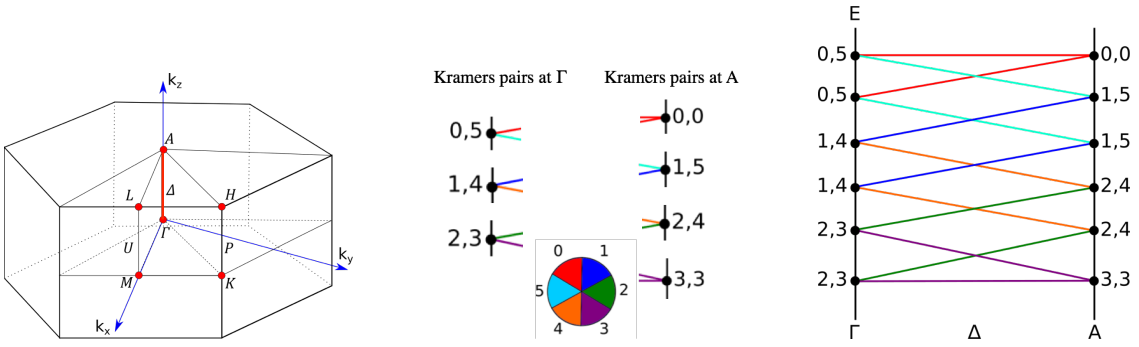


(a) (b) (c)

FIG. 12: *Weyl points with accordion dispersion.* (a) Hexagonal BZ with the symmetry labels for the high-symmetry lines and points indicated. (b) Kramers pairs at the TRIMs Γ and A. The colors represent the $C_{6,1}$ eigenvalue labels $m$ of the Bloch bands $|\psi_m(\boldsymbol{k})\rangle$, see Eq. (3.17). (c) Band connectivity diagram along the Γ-Δ-A line for SG 178.

### 2. *Weyl points protected by six-fold screw rotation*

As a second example we consider Weyl points which occur in the hexagonal SG $P6_122$ (No. 178). This SG contains a sixfold screw rotation of the form

$$C_{6,p=1} \ : \ (x,y,z) \to (x-y,x,z+\tfrac{1}{6})(\tfrac{\sqrt{3}}{2}\sigma_0 - \tfrac{i}{2}\sigma_z), \tag{3.16}$$

which combines a 60 degree rotation with a translation by 1/6-th of the lattice vector in the $z$ direction. The Pauli matrices in the second brackets represent the spin part that needs to be included for Bloch electrons with spin-orbit coupling. Applying the screw rotation six times give minus a unit translation in the $z$ direction, i.e., $-\hat{T}_z$, where the minus sign is from the spin part. The screw rotation leaves the Γ-Δ-$A$ line invariant, which connects the point at the center of the BZ to the A point at the top surface of the BZ, see Fig. 12.

*a. Symmetry eigenvalues.* Within the invariant line Γ-Δ-$A$ we can label the Bloch states by the eigenvalues of $C_{6,1}$, i.e.,

$$C_{6,1}\,|\psi_m(\boldsymbol{k})\rangle = e^{i\pi(2m+1)/6}e^{-ik_z/6}\,|\psi_m(\boldsymbol{k})\rangle\,, \tag{3.17}$$

which follows from the first line of Eq. (3.3) with $p=1$, $n=6$, and $\boldsymbol{a}=(0,0,1)$. In Eq. (3.17) the eigenvalue label $m$ runs from 0 to 5.

Since we study nonmagnetic systems, we need to consider also the role of time-reversal symmetry, Eq. (3.11). Time-reversal symmetry leaves invariant the Γ point and the M point.

Due to Kramers theorem, time-reversal symmetry enforces twofold degeneracies between bands whose $C_{6,1}$ eigenvalues are complex conjugate pairs. Using Eq. (3.17), we find that at the $\Gamma$ point bands with the eigenvalue labels (0, 5), (1, 4), and (2, 3) form Kramers partners, since $C_{6,1}\,|\psi_0(\Gamma)\rangle = e^{i\pi/6}\,|\psi_0(\Gamma)\rangle$, $C_{6,1}\,|\psi_5(\Gamma)\rangle = e^{i\pi\frac{11}{6}}\,|\psi_5(\Gamma)\rangle$, etc., see Fig. 12(b). Similarly, at the A point we find that bands with the eigenvalue labels (0,0) , (3,3), (1,5), and (2,4) pair up, since, $C_{6,1}\,|\psi_0(A)\rangle = |\psi_0(A)\rangle$, $C_{6,1}\,|\psi_3(A)\rangle = -\,|\psi_3(A)\rangle$, etc. Therefore, as shown in Fig. 12(b), the bands pair up in different ways at the $\Gamma$ and A points. As a consequence, the Kramers pairs must switch partners between $\Gamma$ and $A$, which leads to a nontrivial band connectivity, as displayed in Fig. 12(c). There are twelve bands forming a connected group with an accordion-like dispersion. These twelve bands have to cross at least five times, forming five Weyl point degeneracies. The bands that cross at these Weyl points have different $C_{6,1}$ eigenvalues, which prevents hybridization between them. In addition, the Weyl points are protected by a nonzero Chern number, which gives rise to Fermi arcs at the surface, as demonstrated below in Sec. III B 2 c.

*b. Compatibility relations.* The band connectivity discussed in the previous section [Fig. 12(c)] can also be derived using compatibility relations between irreps. In Sec. III B 1 b we have explained how this is done for SG 190. The derivation for SG 178 proceeds in a very similar way. The double valued irreps and the compatibility relations can be obtained from the programs "REPRESENTATIONS DSG" and "DCOMPREL" from the Bilbao Crystallographic Server [66, 69]. The remaining step is then to connect the irreps at the two TRIMs $\Gamma$ and A through the irreps at the line $\Delta$. This yields a band connectivity diagram that is identical to the one of Fig. 12(c). We leave it to the reader to work this out in detail.

*c. Example material.* We have shown that any material with strong spin-orbit coupling crystallizing in SG 178 exhibits Weyl points with an accordion-like dispersion along the $\Gamma$-$\Delta$-A line. Hence, to find example materials we search for compounds in SG 178 in the ICSD database [60]. We find that $AuF_3$, whose band structure is displayed in Fig. 13(a), has the desired properties. The band structure displays a well separated group of twelve bands $\sim$1.5 eV above the Fermi energy $E_{\mathrm{F}}$. This group of bands shows the predicted Weyl points in a very clear way. Along the $\Gamma$–$\Delta$–A line, which is symmetric under the screw rotation $C_{6,1}$, we observe a group of twelve bands sticking together with an accordion-like dispersion, forming five crossings. Along the M–U–L line, which is invariant under the screw rotation $C_{6,1}^3$, there are groups of four connected bands, with an hourglass dispersion and a single crossing point. (Note that the two bands marked by the red square form an avoided crossing.) The appearance of these hourglass Weyl points is a consequence

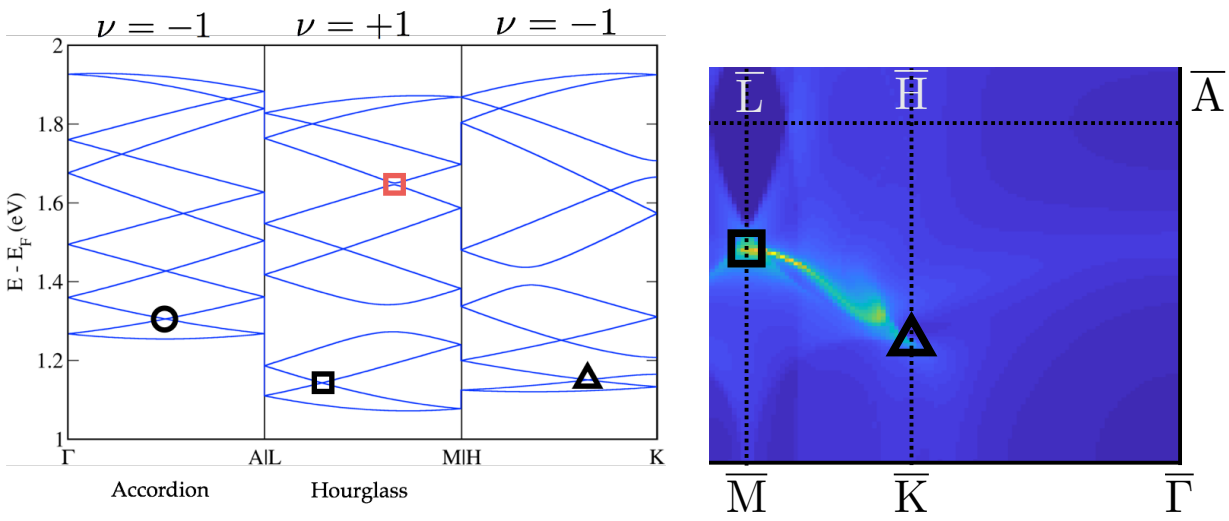


(a) (b)

FIG. 13: *Band structure of $AuF_3$.* (a) First-principle band structure of $AuF_3$ [42]. The band crossings along the Γ–Δ–A and M–U–L lines are symmetry-enforced by the screw rotations $C_{6,1}$ and $C_{6,1}^3$, respectively. (b) Fermi arc surface state at the (010) face of $AuF_3$. Yellow and blue correspond to high and low intensity, respectively.

of the $C_{6,1}^3$ screw rotation, which can be understood using similar arguments as in Sec. III B 2 a.

The topological stability of all these Weyl points is ensured by quantized Chern numbers, which endow the Weyl points with definite chiralities $\nu$. Interestingly, the chiralities of the Weyl points of $AuF_3$ can be infered from symmetry alone, at least up to some overall signs. This can be achieved using the following three observations:

(i) The chiralities of all the Weyl points formed by one pair of bands must add up to zero, due to the fermion doubling theorem [46].

(ii) Weyl points which are mapped onto each other under rotation (and other space group symmetries) must have the same charilities.

(iii) The chiralities $\nu$ can be assumed be either $+1$ or $-1$, since all the bands cross linearly and not quadratically; at least for the $z$ direction [70].

Using these three observations, let us analyze, as an example, the chiralities of the Weyl points formed by the second and third lowest bands in Fig. 13(a) (black open symbols). Looking at the hexagonal BZ in Fig. 12(a), we see that there are three inequivalent Weyl points at the M–U–L

lines which transfrom into each other under rotation. These three Weyl points must therefore all have the same chirality, which we denote by $\nu_{\text{MUL}}$. Similarly, there are two inequivalent Weyl points at the K–P–H lines with chirality $\nu_{\text{KPH}}$, and one Weyl point at the Γ–Δ–A line with chirality $\nu_{\Gamma\Delta\text{A}}$. Hence, the chiralities of these six Weyl points must obey the equation

$$3\nu_{\text{MUL}} + 2\nu_{\text{KPH}} + \nu_{\Gamma\Delta\text{A}} = 0, \tag{3.18}$$

which, up to an overall sign, fully determines the chiralites, i.e., [11]

$$(\nu_{\text{MUL}}, \nu_{\text{KPH}}, \nu_{\Gamma\Delta\text{A}}) = (+1, -1, -1). \tag{3.19}$$

The nontrivial topology exhibited by the Weyl points of $AuF_3$ manifests itself at the surface through arc states, via the bulk-boundary correspondence [5]. These arc states connect Weyl points with opposite chiralities. This is shown in Fig. 13(b), which displays the surface density of states of a semi-infinite $AuF_3$ slab with (010) face at the energy $E - E_{\text{F}} = 1.14$ eV, corresponding to the energy of the second and third lowest bands in Fig. 13(a). We observe that there is an arc state connecting the projected Weyl points of the M–U–L and K–P–H lines, which are marked by the black square and triangle, respectively. This confirms that the arc state connects Weyl points with opposite chiralities, cf. Eq. (3.19).

### *3. Dirac lines protected by off-centered symmetries*

As a last example, we study Dirac lines, which occur in the hexagonal SG $P6_3/m$ (No. 176). This SG contains a glide reflection $\widetilde{M}_z = \{\widetilde{m}_z|\frac{1}{2}\hat{z}\}$, which transforms the spatial coordinates and the spin as

$$\widetilde{M}_z \ : \ (x, y, z) \to (x, y, -z + \tfrac{1}{2}) i\sigma_z, \tag{3.20a}$$

together with an inversion symmetry

$$P \ : \ (x, y, z) \to (-x, -y, -z). \tag{3.20b}$$

[11] It should be noted that the second and third lowest conduction bands can, in principle, also form accidental Weyl points, i.e., Weyls points aways from high-symmetry lines, whose existence is not enforced by symmetry. These accidential Weyl points always come in opposite chirality pairs, such that their contribution to the equation for the chiralities cancels out.

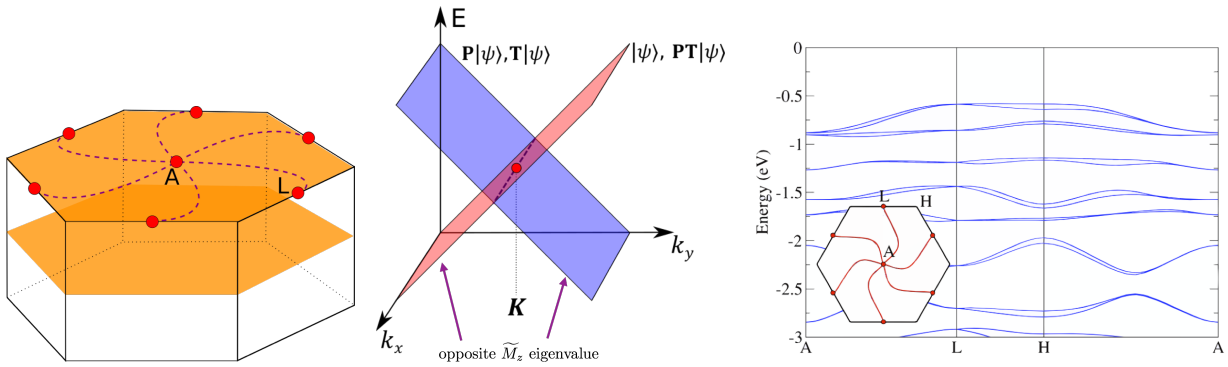


(a) (b) (c)

FIG. 14: *Dirac lines protected by off-centered symmetries.* (a) Fourfold-degenerate Dirac nodal lines connecting the A and L points of the hexagonal BZ. (b) Two Kramers degenerate bands with opposite $\widetilde{M}_z$ eigenvalues cross each other to form a fourfold-degenerate nodal line. (c) Electronic band structure of $LaBr_3$.

These two symmetries form together a pair of so-called off-centered symmetries [39–42]. The Pauli matrix $\sigma_z$ in Eq. (3.20a) represents the spin part, which is relevant for materials with spin-orbit coupling. Note that the translation part $\boldsymbol{t} = \frac{1}{2}\hat{z}$ of the glide reflectioin (3.20a) is perpendicular to the $\widetilde{m}_z$ invariant space (i.e., the $xy$ mirror plane). This type of glide reflection can be transformed into a symmorphic symmetry by a different choice of reference for $\widetilde{m}_z$, i.e., by shifting the origin by $\frac{1}{4}\hat{z}$. However, this shift in origin also affects $P$, leading to a translation part in $P$. Since $\widetilde{M}_z$ and $P$ have different reference points, it is not possible to choose the origin such that both $\widetilde{M}_z$ and $P$ are without translation parts. A pair of two such symmetries with different reference points are called *off-centered symmetries*. We will now show that such off-centered symmetries enforce the existence of fourfold degenerate Dirac nodal-lines.

*a. Symmetry eigenvalues.* The glide reflection (3.20a) leaves two planes in the BZ invariant, namely the $k_x = 0$ plane and the $k_x = \pi$ plane, see Fig. 14(a). Within these planes we can label the Bloch states by the $\widetilde{M}_z$ eigenvalues $\pm i$ (remember that $\widetilde{M}_z^2 = -1$). I.e., we have

$$\widetilde{M}_z \, |\psi_\pm(\boldsymbol{k})\rangle = \pm i \, |\psi_\pm(\boldsymbol{k})\rangle \, . \tag{3.21}$$

Applying the symmetry operators $\widetilde{M}_z$ and $P$ in succesion,

$$(x,y,z) \xrightarrow{P} (-x,-y,-z) \xrightarrow{\widetilde{M}_z} (-x,-y,+z+\tfrac{1}{2})i\sigma_z,$$
$$(x,y,z) \xrightarrow{\widetilde{M}_z} (x,y,-z+\tfrac{1}{2})i\sigma_z \xrightarrow{P} (-x,-y,+z-\tfrac{1}{2})i\sigma_z,$$

we see that $\widetilde{M}_z P$ and $P\widetilde{M}_z$ differ by a unit translation in the $z$ direction ( $\hat{z}$ ). Therefore, we obtain the following commutation relation in momentum space

$$\widetilde{M}_z P \left|\psi_\pm(\boldsymbol{k})\right\rangle = e^{ik_z} P\widetilde{M}_z \left|\psi_\pm(\boldsymbol{k})\right\rangle . \tag{3.22}$$

Hence, the two symmetry operators commute in the $k_z = 0$ plane, while they anticommute in the $k_z = \pi$ plane.

Because we are interested in nonmagnetic systems, we now also need to study the commutation relation between the off-centered symmetries (3.20) and the time-reversal operator $\mathcal{T} = i\sigma_y\mathcal{K}$. Since $\mathcal{T}$ commutes with both $\widetilde{M}_z$ and $P$, we have

$$\widetilde{M}_z P\mathcal{T} \left|\psi_\pm(\boldsymbol{k})\right\rangle = e^{ik_z} P\mathcal{T}\widetilde{M}_z \left|\psi_\pm(\boldsymbol{k})\right\rangle . \tag{3.23}$$

Hence, the Kramers pair $\left|\psi_\pm(\boldsymbol{k})\right\rangle$ and $P\mathcal{T}\left|\psi_\pm(\boldsymbol{k})\right\rangle$ have the same $\widetilde{M}_z$ eigenvalues for $k_z = \pi$, since $\widetilde{M}_z \left[PT\left|\psi_\pm(\boldsymbol{k})\right\rangle\right] = -PT\left[\pm i\left|\psi_\pm(\boldsymbol{k})\right\rangle\right] = \pm iPT\left|\psi_\pm(\boldsymbol{k})\right\rangle$, while for $k_z = 0$, they have opposite $\widetilde{M}_z$ eigenvalues. Therefore, if two bands with opposite $\widetilde{M}_z$ eigenvalues cross within the $k_z = \pi$ plane, they form a protected line crossing with fourfold degeneracy. For $k_z = 0$, however, the bands can hybridize and there is no protected crossing possible.

Such a fourfold degenerate nodal line is in fact required to exist by symmetry alone, i.e., it occurs in any material with the off-centered symmetries $(\widetilde{M}_z, P)$. To see this, let us consider the degeneracies at the two TRIMs A and L within the $k_z = \pi$ plane. At these TRIMs the Bloch states form quartets of four degenerate states with the $\widetilde{M}_z$ eigenvalues

$$\widetilde{M}_z \left|\psi_\pm(\boldsymbol{K})\right\rangle = \pm i \left|\psi_\pm(\boldsymbol{K})\right\rangle , \tag{3.24a}$$

$$\widetilde{M}_z P \left|\psi_\pm(\boldsymbol{K})\right\rangle = \mp iP \left|\psi_\pm(\boldsymbol{K})\right\rangle , \tag{3.24b}$$

$$\widetilde{M}_z \mathcal{T} \left|\psi_\pm(\boldsymbol{K})\right\rangle = \mp i\mathcal{T} \left|\psi_\pm(\boldsymbol{K})\right\rangle , \tag{3.24c}$$

$$\widetilde{M}_z P\mathcal{T} \left|\psi_\pm(\boldsymbol{K})\right\rangle = \pm iP\mathcal{T} \left|\psi_\pm(\boldsymbol{K})\right\rangle , \tag{3.24d}$$

where $\boldsymbol{K} \in \{\mathrm{A}, \mathrm{L}\}$. These four Bloch states are mutually orthogonal to each other, since they either have opposite $\widetilde{M}_z$ eigenvalues or are Kramers partners. As we move away from the TRIMs, the Bloch bands become twofold degenerate in general. We find, however, that the two energetically degenerate states $\left|\psi_\pm(\boldsymbol{K} + \boldsymbol{k})\right\rangle$ and $\left|\psi_\pm(\boldsymbol{K} - \boldsymbol{k})\right\rangle$, which are mapped onto each other by $P$ (or by $\mathcal{T}$), have opposite $\widetilde{M}_z$ eigenvalues. This leads to a band structure, whose $\widetilde{M}_z$ eigenvalues are inverted with respect to $\boldsymbol{K}$, as shown in Fig. 14(b). Since the Bloch bands are smooth functions

of $\boldsymbol{k}$, each quartet of Bloch states at $\boldsymbol{K}$ must therefore be part of a fourfold degenerate nodal line connecting two TRIMs, as illustrated in Fig. 14(a). Note that this fourfold degenerate (i.e., Dirac) nodal line must be symmetric under $\mathcal{T}$ and $P$ and all other point-group symmetries of the SG, but is otherwise free to move within the $k_z = \pi$ plane. That is, the Dirac nodal line is movable, but not removable. Hence, due to the sixfold rotation symmetry of SG 176 the Dirac nodal lines are typically shaped like a star [see Fig. 14(a)].

*b. Example material.* We have shown that all materials crystallizing in SG 176 have star-shaped nodal lines within the $k_z = \pi$ plane. In order to look for materials we go again to ICSD database [60] and find the compound $LaBr_3$. The first-principles band structure of $LaBr_3$ is shown in Fig. 14(c). All bands of $LaBr_3$ are Kramers degenerate, since SG 176 contains a $P\mathcal{T}$ symmetry which squares to $-1$, see Appendix A. Along the A–L–H–A path, within the $k_z = \pi$ plane, there are groups of two Kramers degenerate bands which cross each other several times. These band crossings are part of a fourfold degenerate Dirac nodal line, whose shape resembles a star [inset of Fig. 14(c)]. The nontrivial topology of these Dirac nodal lines are expected to give rise to double drumhead surface states, via a bulk-boundary correspondence.

### C. Filling constraints for the existence of band insulators

It follows from band theory that, in the presence of time-reversal symmetry, a noninteracting band insulator can form only if the electron filling $\nu$ is an even integer, i.e., $\nu \in 2\mathbb{N}$ [12]. That is, materials with $\nu \notin 2\mathbb{N}$ must necessarily be (semi-)metals. However, in materials with nonsymmorphic symmetries these filling constraints for the existence of band insulators are tightened [31, 71]. I.e., nonsymmorphic symmetries forbid the existence of band insulators even when $\nu \in 2\mathbb{N}$. This is because nonsymmorphic symmetries generally enforce extra band crossings, leading to groups of more than two connected bands, as we have seen in Sec. III B. Hence, as a byproduct of our analysis, we can obtain the tightened filling constraints for the existence of band insulators.
For example, for SG 178 we find that along the Γ–Δ–A line twelve bands form a connected group, see Fig. 12(c). Hence, for a material in SG 178 to be an insulator, these groups of bands must be fully filled, i.e., the electron filling $\nu$ must be an element of $12\mathbb{N}$. This tightened filling constraint for SG 178 is in agreement with the recent literature [72, 73].

[12] The electron filling is defined as the number of electrons per primitive unit cells.

**Acknowledgments**

The material presented in these lectures is based upon works I did together with my colleagues and collaboratiors, in particular Ching-Kai Chiu, Yang-hao Chan, Yuxin Zhao, Philip Brydon, Carsten Timm, Jonathan Zhang, Wenbin Rui, Andreas Leonhardt, Leslie Schoop, and Maia Vergniory.

**Appendix A: Kramers theorem**

Kramers theorem states that for every eigenstate $|\psi\rangle$ of a time-reversal symmetric Hamiltonian $H$ with half-integer total spin $S$, there exists another eigenstate of $H$, namely $\mathcal{T}|\psi\rangle$, with the same energy, but orthogonal to $|\psi\rangle$, i.e.,

$$H|\psi\rangle = E|\psi\rangle \quad \Rightarrow \quad H\mathcal{T}|\psi\rangle = E\mathcal{T}|\psi\rangle \quad \text{with} \quad \langle\psi|\mathcal{T}|\psi\rangle = 0. \tag{A1}$$

That is, every energy state is (at least) doubly degenerate for time-reversal symmetric systems with half-integer spin.

The proof follows from the fact that:

(i) for systems with half-integer total spin $S$ the time-reversal operator squares to $-1$, i.e., $\mathcal{T}^2 = \exp(2\pi i S) = -1$.

(ii) the antiunitarity of $\mathcal{T}$, i.e., the time-reversal operator can be written as $\mathcal{T} = U\mathcal{K}$, where $U$ is a unitary matrix and $\mathcal{K}$ is the complex conjugation operator.

Since $\mathcal{T}$ commutes with $H$ [cf. Eq. (3.11)], we have $H\mathcal{T}|\psi\rangle = \mathcal{T}H|\psi\rangle = E\mathcal{T}|\psi\rangle$. It remains to be shown that $\mathcal{T}|\psi\rangle$ is linearly independent of $|\psi\rangle$, i.e., $\langle\psi|\mathcal{T}|\psi\rangle = 0$.

From points (i) and (ii) above it follows that $\mathcal{T}^2 = U\mathcal{K}U\mathcal{K} = UU^* = -1$. Since $U$ is unitary we find $U^* = -U^\dagger$ and therefore

$$U = -U^T. \tag{A2}$$

We now write the scalar product $\langle\psi|\mathcal{T}|\psi\rangle$ in explicit form,

$$\begin{aligned}
\langle\psi|\mathcal{T}|\psi\rangle &= \sum_{m,n} \psi_m^* U_{mn} \mathcal{K}\psi_n \\
&= \sum_{m,n} \psi_m^* U_{mn} \psi_n^* \\
&= \sum_{m,n} \psi_n^* (-U_{nm}) \mathcal{K}\psi_m \\
&= -\langle\psi|\mathcal{T}|\psi\rangle = 0.
\end{aligned} \tag{A3}$$

where in the third line we have used Eq. (A2). This completes the proof.

Since Bloch Hamiltonians $H(\boldsymbol{k})$, Eq. (1.1), with spin-orbit coupling are effectively single-particle systems with spin 1/2, the Kramers theorem directly applies to its Bloch states $|\psi(\boldsymbol{k})\rangle$. That is, for every Bloch state $|\psi(\boldsymbol{k})\rangle$ at momentum $\boldsymbol{k}$ with energy $E$, there exists another Bloch state $|\psi(-\boldsymbol{k})\rangle$ at momentum $-\boldsymbol{k}$ with the same energy. If $\boldsymbol{k}$ is a time-reversal invariant momentum (TRIM), then there is a double degeneracy, i.e., a Kramers degeneracy. Furthermore, we note that for Bloch Hamiltonians which are also inversion symmetric, yielding a $P\mathcal{T}$ symmetry which squares to $-1$, all bands are doubly degenerate.

### Appendix B: Explicit construction of gamma matrices

Explicit expressions for the gamma matrices can be obtained via the spinor representations of $\mathrm{SO}(N)$[74, 75]. The $SO(N)$ generators $M_{jk}$ are expressed in terms of gamma matrices via

$$M_{jk} = -\frac{i}{4}\left[\Gamma^j_{(N)}, \Gamma^k_{(N)}\right], \tag{B1}$$

where $\{\Gamma^a_{(N)}\}_{a=1,\ldots,N}$ are gamma matrices, satisfying $\{\Gamma^j_{(N)}, \Gamma^k_{(N)}\} = 2\delta_{jk}$, with $j, k = 1, \ldots, N$. For $N$ odd, i.e., $N = 2n+1$, one finds that $\mathrm{SO}(2n+1)$ has a $2^n$-dimensional irreducible spinor representation. The gamma matrices in the Dirac representation for $N = 2n+1$ are defined recursively by [74, 75]

$$\begin{aligned}
\Gamma^a_{(2n+1)} &= \Gamma^a_{(2n-1)} \otimes \sigma_3, \quad a = 1, \cdots, 2n-2, \\
\Gamma^{2n-1}_{(2n+1)} &= I_{2^{n-1}} \otimes \sigma_1, \\
\Gamma^{2n}_{(2n+1)} &= I_{2^{n-1}} \otimes \sigma_2, \\
\Gamma^{2n+1}_{(2n+1)} &= (-i)^n \Gamma^1_{(2n+1)} \Gamma^2_{(2n+1)} \cdots \Gamma^{2n}_{(2n+1)},
\end{aligned} \tag{B2}$$

where $I_{2^{n-1}}$ is the $2^{n-1} \times 2^{n-1}$ identity matrix. The gamma matrices in the Dirac representation for $N = 2n$ are constructed in the same way, but by leaving out $\Gamma^{2n+1}_{(2n+1)}$, i.e., $\Gamma^a_{(2n)} = \Gamma^a_{(2n+1)}$, with $a = 1, \cdots, 2n$.

To be more explicit,

$$\begin{aligned}
\Gamma^1_{(2n+1)} &= \sigma_1 \otimes \underbrace{\sigma_3 \otimes \cdots \otimes \sigma_3}_{n-1}, \\
\Gamma^2_{(2n+1)} &= \sigma_2 \otimes \underbrace{\sigma_3 \otimes \cdots \otimes \sigma_3}_{n-1}, \\
\Gamma^3_{(2n+1)} &= \sigma_0 \otimes \sigma_1 \otimes \underbrace{\sigma_3 \otimes \cdots \otimes \sigma_3}_{n-2}, \\
\Gamma^4_{(2n+1)} &= \sigma_0 \otimes \sigma_2 \otimes \underbrace{\sigma_3 \otimes \cdots \otimes \sigma_3}_{n-2}, \\
&\vdots \\
\Gamma^{2n-1}_{(2n+1)} &= \underbrace{\sigma_0 \otimes \cdots \otimes \sigma_0}_{n-1} \otimes \sigma_1, \\
\Gamma^{2n}_{(2n+1)} &= \underbrace{\sigma_0 \otimes \cdots \otimes \sigma_0}_{n-1} \otimes \sigma_2,
\end{aligned} \tag{B3}$$

and

$$\Gamma^{2n+1}_{(2n+1)} = \underbrace{\sigma_3 \otimes \cdots \otimes \sigma_3}_{n}. \tag{B4}$$

From this explicit construction of the gamma matrices, we infer that $\Gamma^{1,3,\cdots,2n+1}_{(2n+1)}$ are all real, and $\Gamma^{2,4,\cdots,2n}_{(2n+1)}$ are purely imaginary.

### Appendix C: Computation of the Berry phase

The Berry phase can be obtained by the phase of the Wilson loop, i.e., $P_{\mathcal{L}} = i \ln \mathcal{W}_{\mathcal{L}}$, where the Wilson loop is defined as

$$\mathcal{W}_{\mathcal{L}} = \exp\left[-\int_{\mathcal{L}} dl \cdot \boldsymbol{A}(\boldsymbol{k})\right], \tag{C1}$$

with the Berry connection $\boldsymbol{A}_{j,k}(\boldsymbol{k}) = \langle u_j(\boldsymbol{k})| \nabla_{\boldsymbol{k}} |u_k(\boldsymbol{k})\rangle$ , which is a matrix with dimension equal to the number of occupied bands. The Wilson loop can be computed from the the Berry link variable on a momentum-space lattice [56]

$$\mathcal{U}_{\mathcal{L}}(\boldsymbol{k}) = \frac{U^\dagger(\boldsymbol{k}) U(\boldsymbol{k} + \delta \boldsymbol{k}_{\mathcal{L}})}{|U^\dagger(\boldsymbol{k}) U(\boldsymbol{k} + \delta \boldsymbol{k}_{\mathcal{L}}|}, \tag{C2}$$

where $U(\boldsymbol{k})$ is the matrix of occupied eigenstates at momentum $\boldsymbol{k}$. The Wilson loop is the product of $\mathcal{U}_{\mathcal{L}}(\boldsymbol{k})$ along a closed path in momentum space, i.e.,

$$\mathcal{W}_{\mathcal{L}} = \prod_{\boldsymbol{k} \in \mathcal{L}} U_{\mathcal{L}}(\boldsymbol{k}) = U_{\mathcal{L}}(\boldsymbol{k}_0) U_{\mathcal{L}}(\boldsymbol{k}_0 + \delta \boldsymbol{k}_{\mathcal{L}}) U_{\mathcal{L}}(\boldsymbol{k}_0 + 2\delta \boldsymbol{k}_{\mathcal{L}}) \ldots U_{\mathcal{L}}(\boldsymbol{k}_N). \tag{C3}$$

Eq. (C3) can be evaluated numerically in an efficient manner.

---


[1] J. von Neumann and E. Wigner, Z. Physik **30**, 467 (1929).

[2] C.-K. Chiu, J. C. Y. Teo, A. P. Schnyder, and S. Ryu, Rev. Mod. Phys. **88**, 035005 (2016).

[3] G. E. Volovik, *Topology of quantum vacuum*, Lecture Notes in Physics, Vol. 870 (Springer Berlin, 2013) pp. 343–383.

[4] G. E. Volovik, Lect. Notes Phys. **718**, 31 (2007).

[5] N. P. Armitage, E. J. Mele, and A. Vishwanath, ArXiv e-prints (2017), arXiv:1705.01111 [cond-mat.str-el] .

[6] A. Burkov, Annual Review of Condensed Matter Physics **9**, 359 (2018), https://doi.org/10.1146/annurev-conmatphys-033117-054129 .

[7] S.-Y. Yang, H. Yang, E. Derunova, S. S. P. Parkin, B. Yan, and M. N. Ali, ArXiv e-prints (2017), arXiv:1707.04523 [cond-mat.mtrl-sci] .

[8] X. Wan, A. M. Turner, A. Vishwanath, and S. Y. Savrasov, Phys. Rev. B **83**, 205101 (2011).

[9] A. A. Burkov, M. D. Hook, and L. Balents, Phys. Rev. B **84**, 235126 (2011).

[10] S.-Y. Xu, C. Liu, S. K. Kushwaha, R. Sankar, J. W. Krizan, I. Belopolski, M. Neupane, G. Bian, N. Alidoust, T.-R. Chang, H.-T. Jeng, C.-Y. Huang, W.-F. Tsai, H. Lin, P. P. Shibayev, F.-C. Chou, R. J. Cava, and M. Z. Hasan, Science **347**, 294 (2015), http://science.sciencemag.org/content/347/6219/294.full.pdf .

[11] S.-M. Huang, S.-Y. Xu, I. Belopolski, C.-C. Lee, G. Chang, B. Wang, N. Alidoust, G. Bian, M. Neupane, C. Zhang, S. Jia, A. Bansil, H. Lin, and M. Z. Hasan, Nature Communications **6** (2015).

[12] Y.-H. Chan, C.-K. Chiu, M. Y. Chou, and A. P. Schnyder, Phys. Rev. B **93**, 205132 (2016).

[13] G. Bian, T.-R. Chang, R. Sankar, S.-Y. Xu, H. Zheng, T. Neupert, C.-K. Chiu, S.-M. Huang, G. Chang, I. Belopolski, D. S. Sanchez, M. Neupane, N. Alidoust, C. Liu, B. Wang, C.-C. Lee, H.-T. Jeng, C. Zhang, Z. Yuan, S. Jia, A. Bansil, F. Chou, H. Lin, and M. Z. Hasan, Nature Communications **7** (2016).

[14] G. Bian, T.-R. Chang, H. Zheng, S. Velury, S.-Y. Xu, T. Neupert, C.-K. Chiu, S.-M. Huang, D. S. Sanchez, I. Belopolski, N. Alidoust, P.-J. Chen, G. Chang, A. Bansil, H.-T. Jeng, H. Lin, and M. Z. Hasan, Phys. Rev. B **93**, 121113 (2016).

[15] W. B. Rui, Y. X. Zhao, and A. P. Schnyder, Phys. Rev. B **97**, 161113 (2018).

[16] T. BzduÅ!'ek, Q. Wu, A. RÃegg, M. Sigrist, and A. A. Soluyanov, Nature **538**, 75 (2016).

[17] Z. Shi, M. Wang, and J. Wu, Applied Physics Letters **107**, 102403 (2015), https://doi.org/10.1063/1.4930875 .

[18] J. R. Schaibley, H. Yu, G. Clark, P. Rivera, J. S. Ross, K. L. Seyler, W. Yao, and X. Xu, Nature Reviews Materials **1** (2016).

[19] C.-K. Chiu and A. P. Schnyder, Phys. Rev. B **90**, 205136 (2014).

[20] K. Shiozaki and M. Sato, Phys. Rev. B **90**, 165114 (2014).

[21] Y. X. Zhao, A. P. Schnyder, and Z. D. Wang, Phys. Rev. Lett. **116**, 156402 (2016).

[22] A. H. Castro Neto, F. Guinea, N. M. R. Peres, K. S. Novoselov, and A. K. Geim, Rev. Mod. Phys. **81**, 109 (2009).

[23] Z. Wang, Y. Sun, X.-Q. Chen, C. Franchini, G. Xu, H. Weng, X. Dai, and Z. Fang, Phys. Rev. B **85**, 195320 (2012).

[24] C.-K. Chiu and A. P. Schnyder, Journal of Physics: Conference Series **603**, 012002 (2015).

[25] Z. Wang, H. Weng, Q. Wu, X. Dai, and Z. Fang, Phys. Rev. B **88**, 125427 (2013).

[26] L. S. Xie, L. M. Schoop, E. M. Seibel, Q. D. Gibson, W. Xie, and R. J. Cava, APL Mater. **3**, 083602 (2015), http://dx.doi.org/10.1063/1.4926545.

[27] A. Yamakage, Y. Yamakawa, Y. Tanaka, and Y. Okamoto, Journal of the Physical Society of Japan **85**, 013708 (2016), http://dx.doi.org/10.7566/JPSJ.85.013708 .

[28] A. P. Schnyder and P. M. R. Brydon, Journal of Physics: Condensed Matter **27**, 243201 (2015).

[29] B. Beri, Phys. Rev. B **81**, 134515 (2010).

[30] M. Sato, Phys. Rev. B **73**, 214502 (2006).

[31] S. M. Young, S. Zaheer, J. C. Y. Teo, C. L. Kane, E. J. Mele, and A. M. Rappe, Phys. Rev. Lett. **108**, 140405 (2012).

[32] L. M. Schoop, M. N. Ali, C. StraÃ?er, A. Topp, A. Varykhalov, D. Marchenko, V. Duppel, S. S. P. Parkin, B. V. Lotsch, and C. R. Ast, Nature Communications **7** (2016).

[33] Y. X. Zhao and A. P. Schnyder, Phys. Rev. B **94**, 195109 (2016).

[34] L. Michel and J. Zak, Phys. Rev. B **59**, 5998 (1999).

[35] S. M. Young and C. L. Kane, Phys. Rev. Lett. **115**, 126803 (2015).

[36] A. Alexandradinata, Z. Wang, and B. A. Bernevig, Phys. Rev. X **6**, 021008 (2016).

[37] A. Furusaki, Science Bulletin **62**, 788 (2017).

[38] R. Takahashi, M. Hirayama, and S. Murakami, Phys. Rev. B **96**, 155206 (2017).

[39] B.-J. Yang, T. A. Bojesen, T. Morimoto, and A. Furusaki, Phys. Rev. B **95**, 075135 (2017).

[40] C. Fang, Y. Chen, H.-Y. Kee, and L. Fu, Phys. Rev. B **92**, 081201 (2015).

[41] M. Malard, P. E. de Brito, S. Ostlund, and H. Johannesson, ArXiv e-prints (2018), arXiv:1804.09736 [cond-mat.str-el] .

[42] J. Zhang, Y.-H. Chan, C.-K. Chiu, M. G. Vergniory, L. M. Schoop, and A. P. Schnyder, Phys. Rev. Materials **2**, 074201 (2018).

[43] J. Singleton, *Band Theory and Electronic Properties of Solids*, Oxford Master Series in Condensed Matter Physics (Oxford University Press, 2001).

[44] T. Ozawa, H. M. Price, A. Amo, N. Goldman, M. Hafezi, L. Lu, M. Rechtsman, D. Schuster, J. Simon, O. Zilberberg, and I. Carusotto, ArXiv e-prints (2018), arXiv:1802.04173 [physics.optics] .

[45] K. Li, C. Li, J. Hu, Y. Li, and C. Fang, Phys. Rev. Lett. **119**, 247202 (2017).

[46] H. Nielsen and M. Ninomiya, Nuclear Physics B **185**, 20 (1981).

[47] C.-K. Chiu, H. Yao, and S. Ryu, Phys. Rev. B **88**, 075142 (2013).

[48] C.-K. Chiu, ArXiv e-prints (2014), arXiv:1410.1117 [cond-mat.mes-hall] .

[49] T. Morimoto and A. Furusaki, Phys. Rev. B **88**, 125129 (2013).

[50] A. P. Schnyder, S. Ryu, A. Furusaki, and A. W. W. Ludwig, Phys. Rev. B **78**, 195125 (2008).

[51] M. R. Zirnbauer, Journal of Mathematical Physics **37**, 4986 (1996), https://doi.org/10.1063/1.531675 .

[52] A. Altland and M. R. Zirnbauer, Phys. Rev. B **55**, 1142 (1997).

[53] Y. X. Zhao and Z. D. Wang, Phys. Rev. Lett. **110**, 240404 (2013).

[54] T. L. Hughes, E. Prodan, and B. A. Bernevig, Phys. Rev. B **83**, 245132 (2011).

[55] M. Nakahara, *Geometry, Topology and Physics*, 2nd ed. (Tailor & Francis, New York, 2003).

[56] A. Yamamoto, Phys. Rev. Lett. **117**, 052001 (2016).

[57] A. Dauphin, M. Mller, and M. A. Martin-Delgado, New Journal of Physics **16**, 073016 (2014).

[58] A. Alexandradinata and B. A. Bernevig, Phys. Rev. B **93**, 205104 (2016).

[59] A. Bouhon and A. M. Black-Schaffer, ArXiv e-prints (2017), arXiv:1710.04871 [cond-mat.mtrl-sci] .

[60] Https://icsd.fiz-karlsruhe.de/.

[61] S. Curtarolo, W. Setyawan, S. Wang, J. Xue, K. Yang, R. H. Taylor, L. J. Nelson, G. L. Hart, S. Sanvito, M. Buongiorno-Nardelli, N. Mingo, and O. Levy, Computational Materials Science **58**, 227 (2012).

[62] A. Jain, S. P. Ong, G. Hautier, W. Chen, W. D. Richards, S. Dacek, S. Cholia, D. Gunter, D. Skinner,

G. Ceder, and K. a. Persson, APL Materials **1**, 011002 (2013).

[63] "Materials Project," ().

[64] (), http://materiae.iphy.ac.cn/.

[65] J. Kruthoff, J. de Boer, J. van Wezel, C. L. Kane, and R.-J. Slager, Phys. Rev. X **7**, 041069 (2017).

[66] L. Elcoro, B. Bradlyn, Z. Wang, M. G. Vergniory, J. Cano, C. Felser, B. A. Bernevig, D. Orobengoa, G. de la Flor, and M. I. Aroyo, Journal of Applied Crystallography **50**, 1457 (2017).

[67] C. Bradley and A. P. Cracknell, *The Mathematical Theory of Symmetry in Solids: Representation theory for point groups and space groups* (Clarendon Press, Oxford, 1972).

[68] S. C. Miller and W. F. Love, *Tables of Irreducible Representations of Space Groups and Co-representations of Magnetic Groups* (Boulder: Pruett, 1967).

[69] M. G. Vergniory, L. Elcoro, Z. Wang, J. Cano, C. Felser, M. I. Aroyo, B. A. Bernevig, and B. Bradlyn, Phys. Rev. E **96**, 023310 (2017).

[70] S.-M. Huang, S.-Y. Xu, I. Belopolski, C.-C. Lee, G. Chang, T.-R. Chang, B. Wang, N. Alidoust, G. Bian, M. Neupane, D. Sanchez, H. Zheng, H.-T. Jeng, A. Bansil, T. Neupert, H. Lin, and M. Z. Hasan, Proceedings of the National Academy of Sciences **113**, 1180 (2016), http://www.pnas.org/content/113/5/1180.full.pdf .

[71] L. Michel and J. Zak, Physics Reports **341**, 377 (2001), symmetry, invariants, topology.

[72] S. A. Parameswaran, A. M. Turner, D. P. Arovas, and A. Vishwanath, Nature Physics **9** (2013).

[73] H. Watanabe, H. C. Po, M. P. Zaletel, and A. Vishwanath, Phys. Rev. Lett. **117**, 096404 (2016).

[74] J. Polchinski, *String Theory vols 1 and 2* (Cambridge: Cambridge University Press, 1988).

[75] H. Georgi, *Lie Algebras in Particle Physics* (Reading, MA: Perseus Books, 1999).